Eindhoven University of Technology

MASTER

Experimental and numerical analysis of an unsteady pulsatile free shear layer

Reijnierse, C.M.J.

Award date:
1993

Link to publication

Disclaimer
This document contains a student thesis (bachelor's or master's), as authored by a student at Eindhoven University of Technology. Student theses are made available in the TU/e repository upon obtaining the required degree. The grade received is not published on the document as presented in the repository. The required complexity or quality of research of student theses may vary by program, and the required minimum study period may vary in duration.

General rights
Copyright and moral rights for the publications made accessible in the public portal are retained by the authors and/or other copyright owners and it is a condition of accessing publications that users recognise and abide by the legal requirements associated with these rights.

- Users may download and print one copy of any publication from the public portal for the purpose of private study or research.
- You may not further distribute the material or use it for any profit-making activity or commercial gain

Experimental and numerical analysis of an unsteady pulsatile free shear layer

C.M.J. Reijnierse
October 1993

Report no. WFW 93.167 / R-1251-A

Department of Mechanical Engineering
Faculty of Engineering Fundamentals

Coaches: Ir. D.E.M. Palmen
Dr. Ir. F.N. van de Vosse

Supervisors: Prof. Dr. Ir. J.D. Janssen
Dr. Ir. M.E.H. van Dongen

Prefatory note

For writing this report the following setup has been chosen. First an article has been written in which the research done during this project is described. Secondly 6 appendices are presented describing for instance the literature survey, experimental setup and the results more extensively.

Experimental and numerical analysis of an unsteady pulsatile free shear layer

C.M.J. Reijnierse, D.E.M. Palmen, F.N. van de Vosse, J.D. Janssen,
M.E.H. van Dongen[#]

Departments of Mechanical Engineering and Physics[#]
Eindhoven University of Technology
P.O.Box 513, 5600 MB Eindhoven, The Netherlands

Abstract

In order to gain information on the velocity field in two-dimensional unsteady pulsatile free shear layers experimental and numerical investigations have been made. Visualization experiments as well as LDA measurements, using a two component back scatter LDA system, have shown that transient instability occurs. Perturbations arise with natural frequency and seem to grow linearly in first instance. Next a regime of nonlinear growth is seen with rolling-up of the shear layer resulting in pairing of vortices: a subharmonic component is generated. Finally during the steady phase of the flow pulse the perturbations are damped again. The vortices seem to travel with approximately the local velocity. A finite element method has been used for numerical analysis using the inflow conditions obtained from the experimental data. A good agreement with the LDA measurements has been found.

Introduction

Research on blood flow in the carotid artery bifurcation shows that this flow is essentially instationary and three-dimensional (Palmen et al., 1992; Rindt et al., 1990). The flow is characterized by a region of high shear and velocity along the divider wall and a separation zone with low velocity on the non-divider wall, see figure 1.

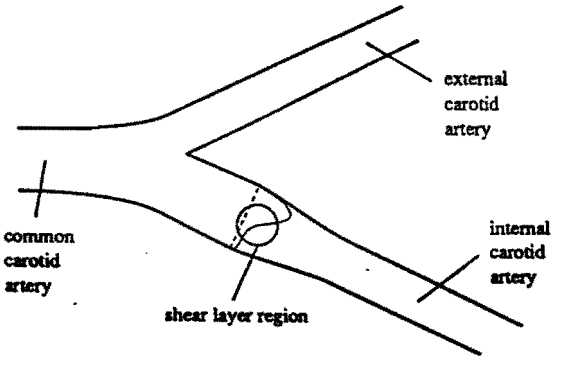

Figure 1. Typical velocity profile in the carotid artery bifurcation.

The interface between the two flow regions may be considered as a time dependent free shear layer. It is assumed that the hydrodynamic stability of the free shear layer plays an important role in the overall flow phenomena that occur in these kinds of bifurcation

geometries.

A free shear layer can also be formed by the merging of two parallel streams of velocity U_1 and U_2 ($U_1>U_2$) initially separated by a thin surface, characterized by the momentum thickness $\Theta(x)$. The flow is schematically drawn in figure 2.

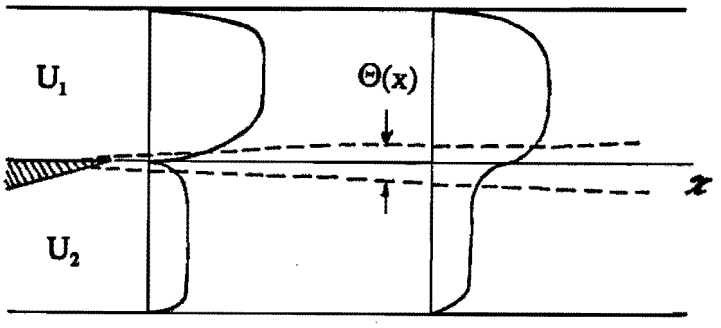

Figure 2. Spatially developing free shear layer, with $\Theta(x)$ the momentum thickness.

Here the developed basic flow has a sort of hyperbolic tangent velocity profile that can be characterized by two dimensionless parameters: the velocity ratio R and Reynoldsnumber Re based on the initial momentum thickness Θ_0:

$$R \equiv \frac{\Delta U}{2\overline{U}} \quad and \quad Re \equiv \frac{\overline{U}\Theta_0}{\nu} \quad with \quad \Delta U = U_1 - U_2 \quad and \quad \overline{U} = \frac{1}{2}(U_1 + U_2)$$

with ν the kinematic viscosity. If the basic flow is taken to be strictly parallel and perturbations are infinitesimal, the perturbation stream function can be cast into the form:

$$\psi(x,y,t) = \phi(y)\exp[i\alpha(x-ct)] + c.c.$$

with complex wavenumber $\alpha = \alpha_1 + i\alpha_2$ and complex wave velocity $c = c_1 + ic_2$.

Previous studies on free shear layers have mainly dealt with unbounded steady flows. Knio and Ghoniem (1990) have concluded that the development of two-dimensional shear layer instability can often be split into three regimes:

* The first regime is a linear regime with linear growth. The amplitude of the perturbation grows exponentially and the form of the perturbation remains unchanged.
* The second regime is a regime in which nonlinear growth occurs, characterized by roll-up and spreading of the shear layer perpendicular to the streamwise direction.
* In the third regime a completion of the growth of the instability takes place, accompanied by pairing of vortex structures. Finally transition to turbulence occurs.

The effect of viscosity on a hyperbolic tangent velocity profile has been investigated by Esch (1957) and Betchov (1963) for temporal instabilities and by Lie et al. (1988) for spatial instabilities. From these studies it was concluded that the instability regime diminishes with increasing viscosity. Viscosity has a damping effect on instability. It was shown that for $\alpha Re>100$ the inviscid theory provided a good approximation of the perturbed free shear layer. Studies of Michalke (1964,1965) in the inviscid limit $Re\rightarrow\infty$ and for R=1 (only one stream is present) showed that the phase velocity c_1 of the perturbation is independent of the wavenumber α for temporal instabilities. The perturbations move with the local velocity of the unperturbed flow. However for spatial instabilities c_1 strongly depends on the frequency of the perturbation wave. Ho and Huerre (1984) came to the same conclusion. Only the perturbation with a frequency corresponding to that of the most amplified wave, travels with local velocity. This frequency is called the natural frequency. Waves with a frequency different from the natural frequency move with a velocity different from the mean velocity. Ho and Huerre (1984) have also studied the influence of different velocity ratios R. It seemed that the natural frequency hardly changed with variations in R. The Strouhal number St defined as:

$$St = \frac{f\Theta}{U} \qquad with \quad f = \frac{\omega}{2\pi}$$

corresponding to the natural frequency was $St_n=0.032$. The maximum spatial growth rate $(\alpha_2\Theta)_{max}$ was seen to increase approximately linear with velocity ratio R. It was also shown that the pairing of vortices is indeed the primary proces governing the streamwise growth of the shear layer (third regime) and that this pairing results in the generation of a subharmonic component. That is: perturbations (vortices) with half the natural frequency occur.

However most studies have dealt with unbounded shear layers, experimental situations will always be bounded. Esch (1957) and Lie et al. (1988) have concluded that the presence of boundaries has a damping effect on the development of instabilities. After all a bounded geometry suggests a maximum perturbation wavelength and therefore a minimum value of wavenumber α. The importance of three-dimensional effects was first mentioned by Miksad (1972). It was seen that three-dimensional deformations appear only in a late state (third regime) resulting in the transition to turbulence where 3D activity dominates the flow.

Whenever is dealt with unsteady flows, the stability analysis gets very complicated. The stability of unsteady flows is a relatively new and unstudied subject and even the meaning of stability is not completely clear, as the magnitude of the basic flow changes substantially with time. For periodically unsteady flows three situations can be distinguished (Davis, 1976):

* The flow is called unstable whenever a perturbation experiences a net growth over every period of the basic flow.
* A flow is called monotonically stable when every perturbation is damped on each moment of the period.
* Transient stability occurs when a perturbation only grows during part of the cycle, reaching a maximum amplitude and is damped again.

Considering the free oscillation of perturbations of the time averaged basic flow, than the essential mechanism of instability of unsteady periodic flows is a resonance between the forced oscillation of the basic flow and these free oscillation when the frequency is half or an integral multiple of the frequency of the forced oscillation (Kelly, 1965; Drazin and Reid, 1981).

In order to gain more information on the instability of perturbed unsteady pulsatile free shear layers in this study the two-dimensional free shear layer has been analysed experimentally and numerically. A model of the physiological flow pulse has been used.

Experimental methods

The fluid circuit

A schematic presentation of the fluid circuit is given in figure 3. The reservoir is filled with water at room temperature. A gear pump (micropump, Verder) is used for the generation of the steady flow component. The unsteady flow component is generated by a computer controlled piston pump (superpump, VSI). Before merging in the channel the two streams pass the settling chamber. The height of the channel is 2H, where H=0.5cm and the width amounts 12H. The tip of the separation plate is also presented in figure 3 and has an angle of approximately 16°. The thickness of the separation plate is H/5.

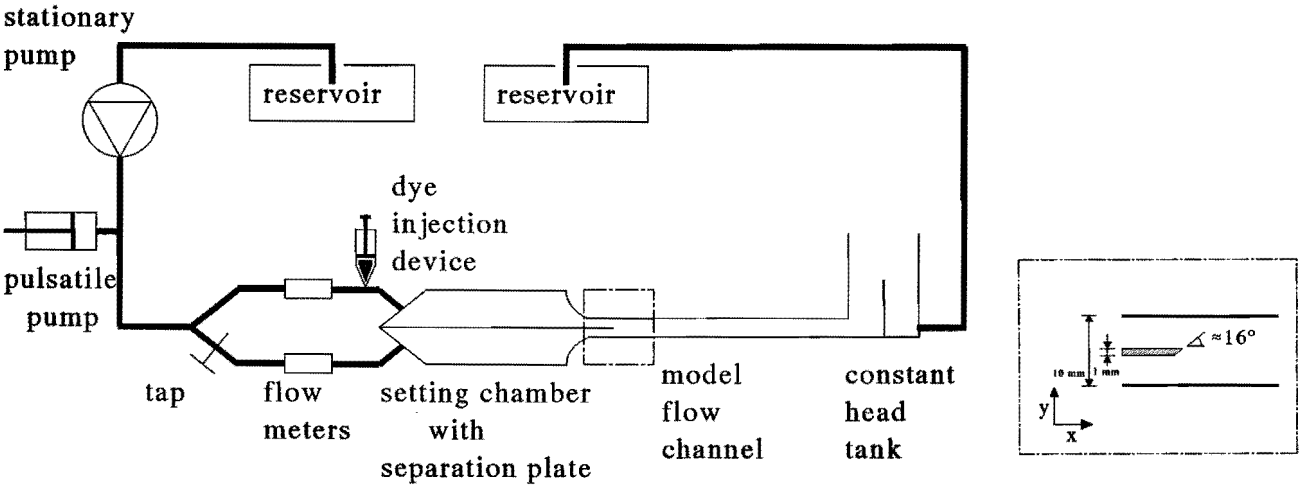

Figure 3. **Schematic representation of the fluid circuit.**

For the visualization experiments fluorescent dye has been injected in the upper flow before entering the settling chamber, having the same density as the fluid so that gravity influences can be neglected. Before the flow reaches the edge of the separation plate the dye has mixed completely with the fluid of the upper flow.

Quantitative velocity measurements have been made by means of a two component fiber optics LDA system in backscatter mode in combination with a Flow Velocity Analyser (58N20, Dantec). A 300 mW Argon-ion laser (5500A, Ion Laser Technology) generates a green laser beam (λ = 488.0 nm) and a blue laser beam (λ = 514.5 nm). With the aid of

glass fibers the light is transmitted to a measuring probe. A front lens with a focal length of 159.8 mm focusses the laser beams to form a measuring volume with dimensions 74 × 74 × 623 μm.

Experimental procedure

The flow pulse used to achieve an unsteady flow is a modeled physiological pulse (see figure 4a). The flow pulse consists of a cosine that lasts 20 percent of the period time, the systolic phase, superimposed on a steady flow component, the diastole. The pulse can be described by the dimensionless parameters: the Reynolds number Re and the Womersley parameter α defined by:

$$Re = \frac{2HU}{\nu} \qquad \alpha = \frac{2H}{2}\sqrt{\frac{\omega}{\nu}}$$

where U is the mean velocity in the flow channel, H is half the height of the channel and ν the kinematic viscosity of the fluid and the angular velocity $\omega=2\pi/T$ with T=4.33 s the period time of the flow pulse. The experiments have been performed for Re_{dias} = 270, Re_{syst} = 1000 and α = 6. The flow ratio between the bottom flow Q_2 and upper flow Q_1 used in the experiments is Q_2:Q_1 = 1:3, see figure 4b. This flow ratio has been chosen for its similarity with the physiological situation. The flow ratio is not constant over one period. During the systole the bottom flow Q_2 increases with respect to the upper flow Q_1. At the end of the systole the flow ratio decreases again and is even smaller than the original 1:3 ratio for some time.

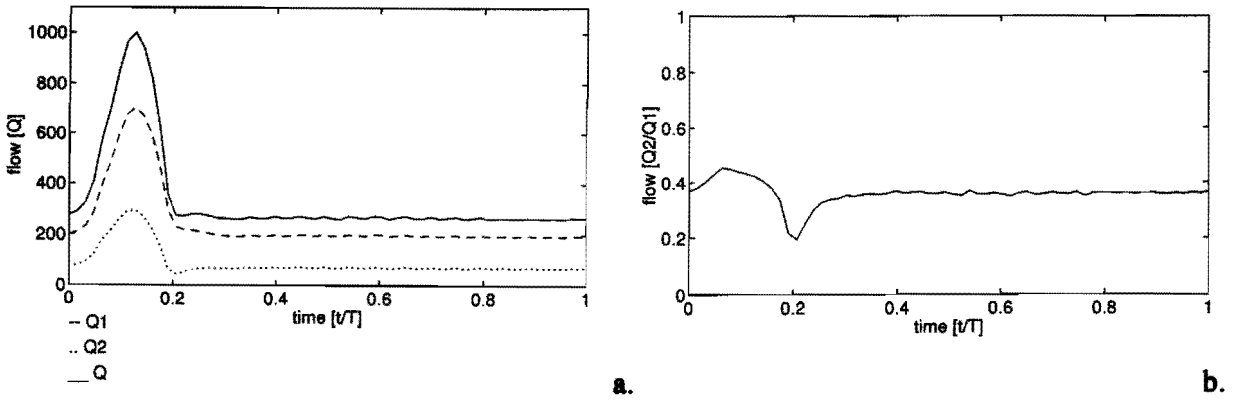

Figure 4. The flow pulse (a) and the flow ratio (b).

Velocities have been measured along the horizontal X- and vertical Y-axis. Figure 5 shows the measuring sites. Y10 for example stands for measurements that have been taken along the Y-axis at 2H (=10 mm) distance from the separation edge. The velocity component in the axial direction has been measured and is called the axial velocity.

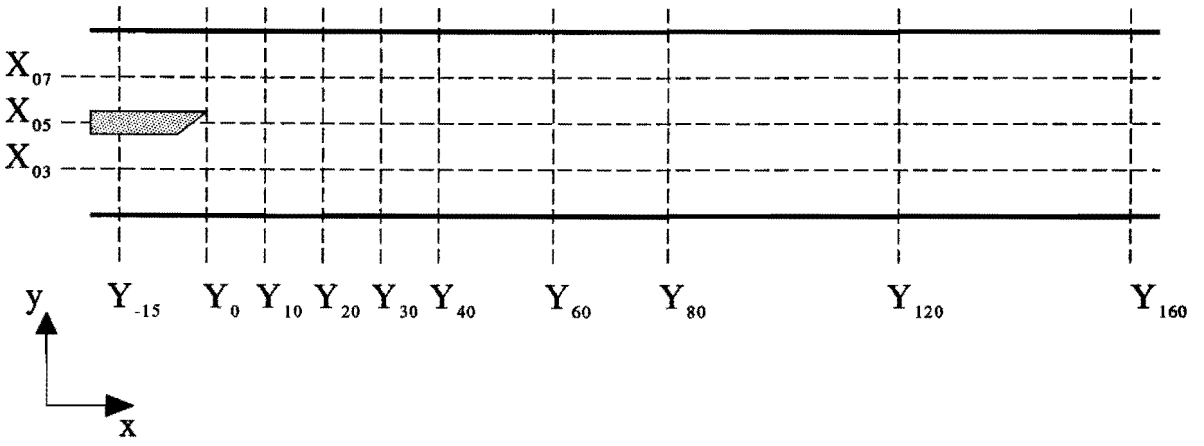

Figure 5. **The measuring sites for the LDA-experiments.**

During 16 periods velocities have been measured at each measuring site. After the separation of the periods, each period is divided into 64 intervals and the velocities in these intervals have been averaged (Gijsen, 1993) to obtain an equidistant set of data in time. Finally the best 9 cycles have been selected to compute the ensemble averaged velocities.

Numerical method

The two dimensional unsteady free shear layer has also been computed numerically using a finite element method. For the time dependent inflow the LDA measurements at site Y00 (see figure 7) have been used. At both walls the no-slip condition is valid. A similar geometry as for the experiments was used. The length of the channel was 30H, where 2H is the height of the channel. The outflow is determined by a zero stress-vector.

The two-dimensional Navier-Stokes equations for incompressible Newtonian fluids are given by the momentum equations together with the continuity equation:

$$\rho \frac{\partial \vec{u}}{\partial t} + \rho(\vec{u}\cdot\nabla)\vec{u} = \rho \vec{f} + \nabla \underline{\sigma} \tag{1}$$

$$\nabla \cdot \vec{u} = 0 \tag{2}$$

where ρ is the density and $\underline{\sigma}$ the Cauchy stress tensor:

$$\sigma_{ij} = -p\delta_{ij} + \eta\left(\frac{\partial u_i}{\partial x_j} + \frac{\partial u_j}{\partial x_i}\right), \qquad (i,j=1,2) \tag{3}$$

with p the pressure, δ_{ij} the Kronecker delta, u_i the i-th component of the velocity and η

the dynamic viscosity.

Spatial discretization

In order to discretize the governing Navier-Stokes equations the standard Galerkin method has been used. The velocity and pressure are approximated by a linear combination of time-independent basis functions ϕ_{in} and ψ_m:

$$\tilde{u}_i = \sum_{n=1}^{N} u_{in}\phi_{in} \qquad (i,j=1,2) \tag{4}$$

$$\tilde{p} = \sum_{m=1}^{M} p_m \psi_m \tag{5}$$

The element used here is the modified Crouzeix-Raviart element, which consists of 7 nodes of which only the central node holds pressure unknowns, the pressure and its derivatives. By eliminating the velocity and pressure derivatives in the central node there are only 13 unknowns per element left (Cuvelier et al., 1986).

This will lead to a set of nonlinear ordinary differential equations (Cuvelier et al., 1986). A penalty function method together with a Newton-Raphson iteration to linearize the convective terms is used. The time-derivative in the discrete Navier-Stokes equations are approximated by a finite difference θ-method (Van de Vosse, 1986). All together this leads to solving the following equations:

first step:

$$\left[\frac{1}{\theta\Delta t}M + S + J(\underline{u}^n) + \frac{1}{\varepsilon}L^T M_p^{-1} L\right]\underline{u}^{n+\theta} = \frac{1}{\theta\Delta t}M\underline{u}^n + \underline{f}^{n+\theta} + \underline{b}^{n+\theta} + N(\underline{u}^n)\underline{u}^n \tag{6}$$

$$\underline{p}^{n+\theta} = \frac{1}{\varepsilon}M_p^{-1} L\underline{u}^{n+\theta} \tag{7}$$

second step:

$$\underline{u}^{n+1} = \frac{1}{\theta}[\underline{u}^{n+\theta} - (1-\theta)\underline{u}^n] \tag{8}$$

Results

Visualization experiments and the numerically computed instantaneous streamlines

The unsteady free shear layer with flow ratio 1:3 has been visualized. The results are given in the video prints at the left-hand side of figure 6. It can be seen that instability first occurs during the decelerating phase of the systole. A small perturbation wave with wavelength λ = 1.6H (0.8 cm) is seen. This perturbation grows during the first part of the diastolic phase and pairing of vortices is observed at t=7T/21, for the wavelength has increased to approximately 3.2H (1.6 cm) and 4H (2.0 cm). The wavelength has been determined with an accuracy of ± 0.5H. Finally the perturbations are damped again. The vortices move with different velocity varying roughly around 1.4 times v(dias) (4.5 cm/s), where v(dias) is the mean velocity at the end of the diastole at site Y00.

The figures at the right-hand side of figure 6 represent the instantaneous streamlines of the finite element computations. As here is dealt with unsteady flows the meaning of streamlines is not completely clear and the plots should be analysed carefully. Nevertheless it is believed that the contourlines of the streamfunction show where the velocity components are constant such that the occurences of disturbances are visible in the instantaneous streamline plots. In figure 6 the ratio of the height and length of the flow channel has been scaled with factor 5. From these plots it is seen that the first oscillations occur during the decelerating phase of the systole with perturbation wavelength of λ = 1.6H (0.8 cm). The perturbations grow during part of the diastole and damp out again. Pairing of vortices occurs further downstream resulting in a wavelength of 3.2H (1.6 cm) and 4H (2.0 cm). The propagation velocity varies from 1.1 to 1.3 v(dias) (3.6 to 4.2 cm/s) during diastole and the propagation velocity is about 2.2 v(dias) (7.1 cm/s) at the systole. Thus the perturbations move approximately with the local velocity of the unperturbed flow.

It is seen that both the visualization as the computed instantaneous streamline plots provide the same information. However only in the streamline plots it was possible to obtain an approximation of the velocity of the perturbations during the systolic phase.

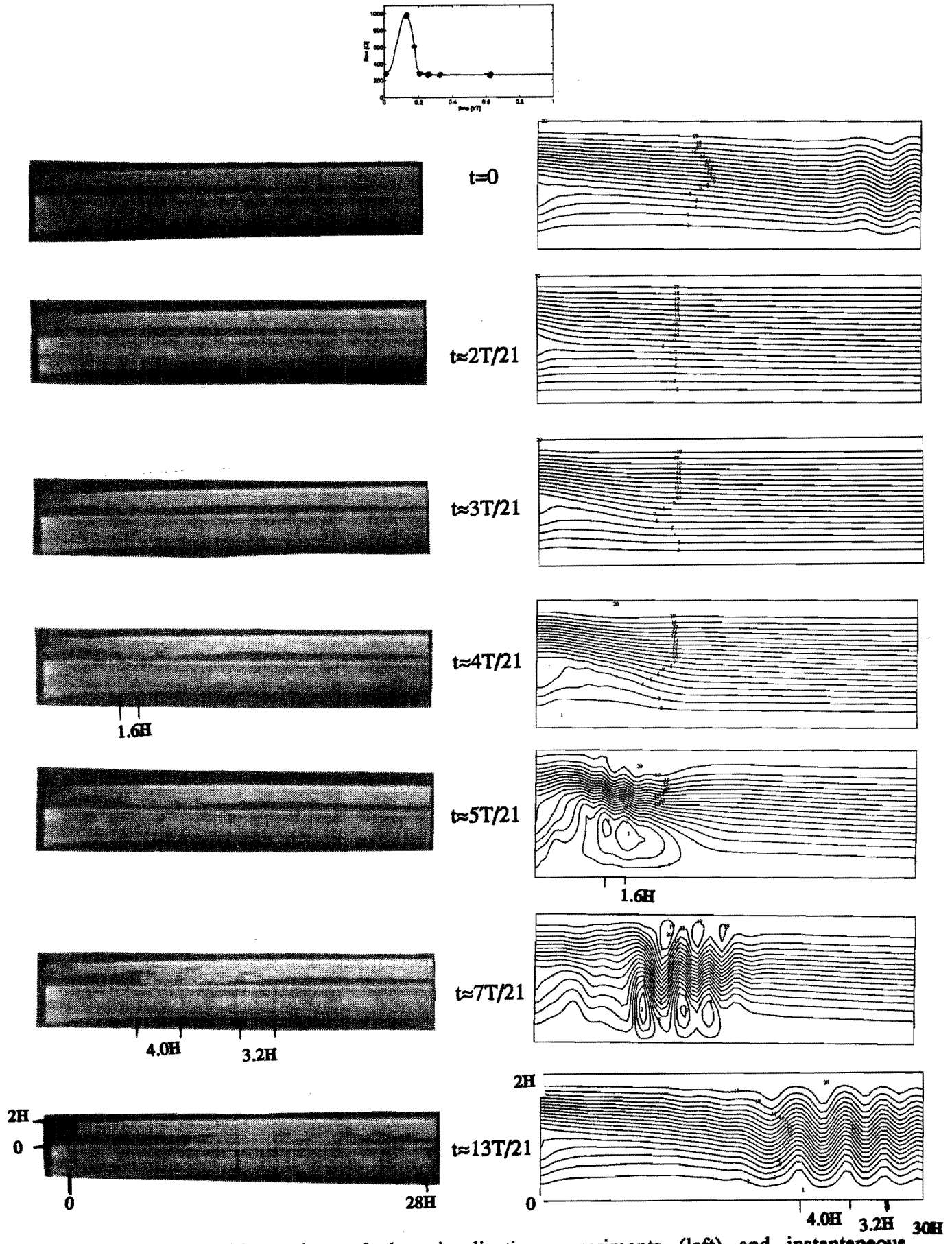

Figure 6. Video prints of the visualization experiments (left) and instantaneous streamline plots for the numerical calculations (right). The ratio of the height and length of the channel is scaled with factor 5. The flow ratio between the bottom and upper flow is 1:3.

LDA measurements and numerical computations

The ensembled averaged signals computed from the velocity data obtained with the LDA system are presented in three dimensional plots. In figure 7 the axial velocities at the end of the tip of the separation plate (site Y00) are represented as a function of time. The parameters time, velocity and position have been made dimensionless respectively by dividing the actual time by the period time of the flow pulse, by computing the ratio of the actual velocity and the mean velocity at Y00 at end diastole v(dias) and by scaling with H, half the height of the flow channel. Position -1 defines the bottom wall of the flow channel and +1 the upper wall. The velocities at the walls are set to 0 cm/s manually.

site Y00 The velocity profiles of the bottom and upper flow are nearly parabolic. The shape of the flow pulse can easily be recognized at this site. However at the beginning of the diastole a small oscillation can be seen. Near the bottom wall a small region of flow reversal is observed.

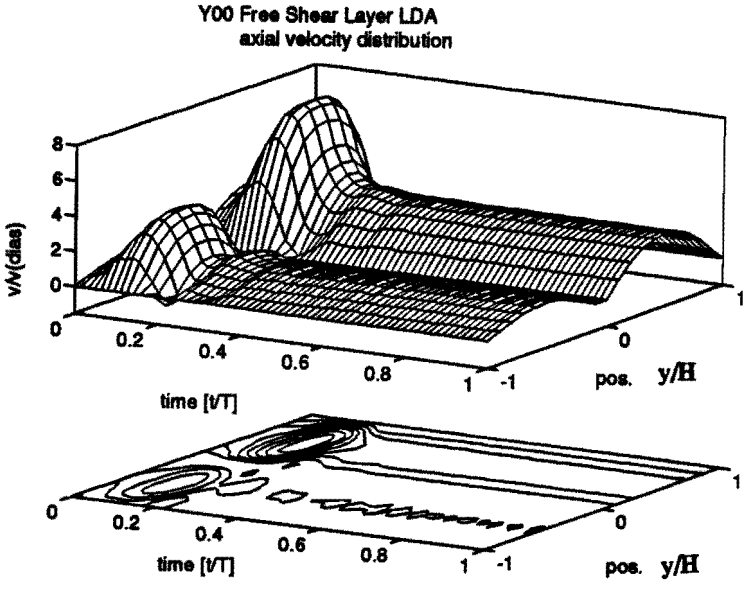

Figure 7. The axial velocities at site Y00 as a function of time.

The axial velocity plots at Y20, Y40 and Y80 are presented in figure 8. At the left-hand side the LDA measurements are shown and at the right-hand side the FEM computations are presented. A short description of the axial velocity fields is given.

site Y20 Near the bottom wall a rather steep velocity gradient during the decelerating phase of the systole can be seen, followed by a region of flow reversal and two small oscillations. In the upper half of the flow channel (at the high velocity region) a gradually decreasing velocity can be observed during the decelerating phase of the systole towards the diastole and a second peak is being developed, followed by two oscillations.

The computations show the same phenomena but the velocity profiles are

smoother. The region of flow reversal near the bottom wall is smaller.

site Y40 Still a rather steep velocity gradient during the decelerating phase of the systole can be seen near the bottom wall, followed by a large region of flow reversal. Also a small region of flow reversal near the upper wall can be observed. Small oscillations are seen in the diastolic phase. The second peak at the high velocity region has grown and moved towards the center of the flow channel. The velocity profiles are not parabolic any more. They have developed like the hyperbolic tangent velocity profile.

For the computations at the upper wall a higher peak can be observed at $t/T \approx 0.35$. The regions of flow reversal are much larger and the perturbation near the bottom wall at $t/T \approx 0.4$ is less large than for the LDA experiments.

site Y80 The peaks of the oscillation are much smaller now and pass this measuring site at a later time of the period after $t/T=0.4$. Velocity peaks in the upper half of the flow channel appear together with velocity dips in the bottom half and reversed. The total velocity profile has nearly developed into a parabolic profile.

Compared to the computions the oscillations in the experiment are smaller, the peaks are lower and less regular.

In figure 9 the axial velocities along the x-axis at site X05 are given as a function of time.

site X05 It is evident that during the decelerating phase of the systole the first oscillations occur within the first 10H (5cm) behind the separation plate. The vortices travel forward with a propagation velocity varying between 1.1 and 1.45 v(dias) (3.6 and 4.7 cm/s). The vortices that arise further downstream move a little faster. The same conclusions can be drawn from the numerical results.

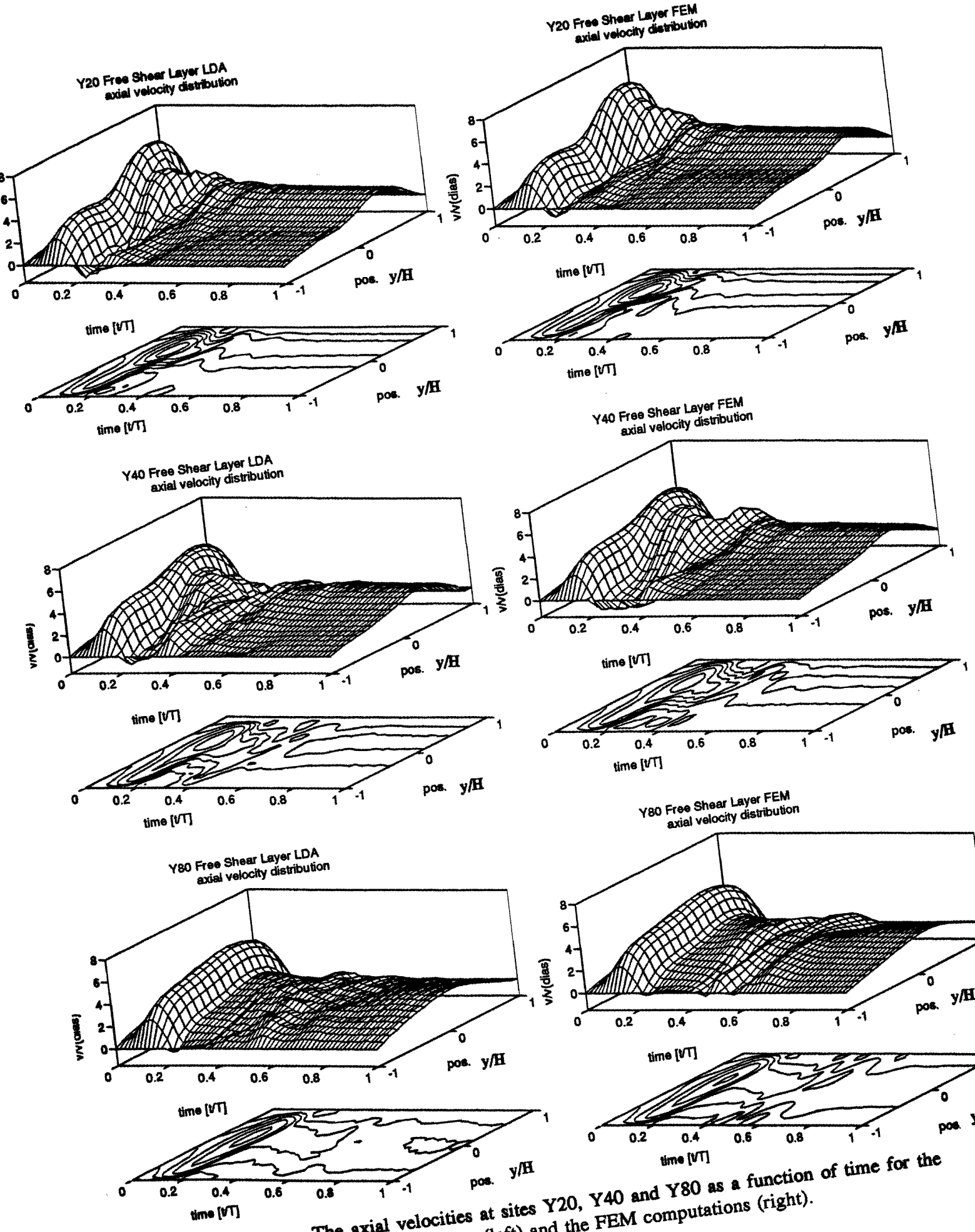

Figure 8. The axial velocities at sites Y20, Y40 and Y80 as a function of time for the LDA measurements (left) and the FEM computations (right).

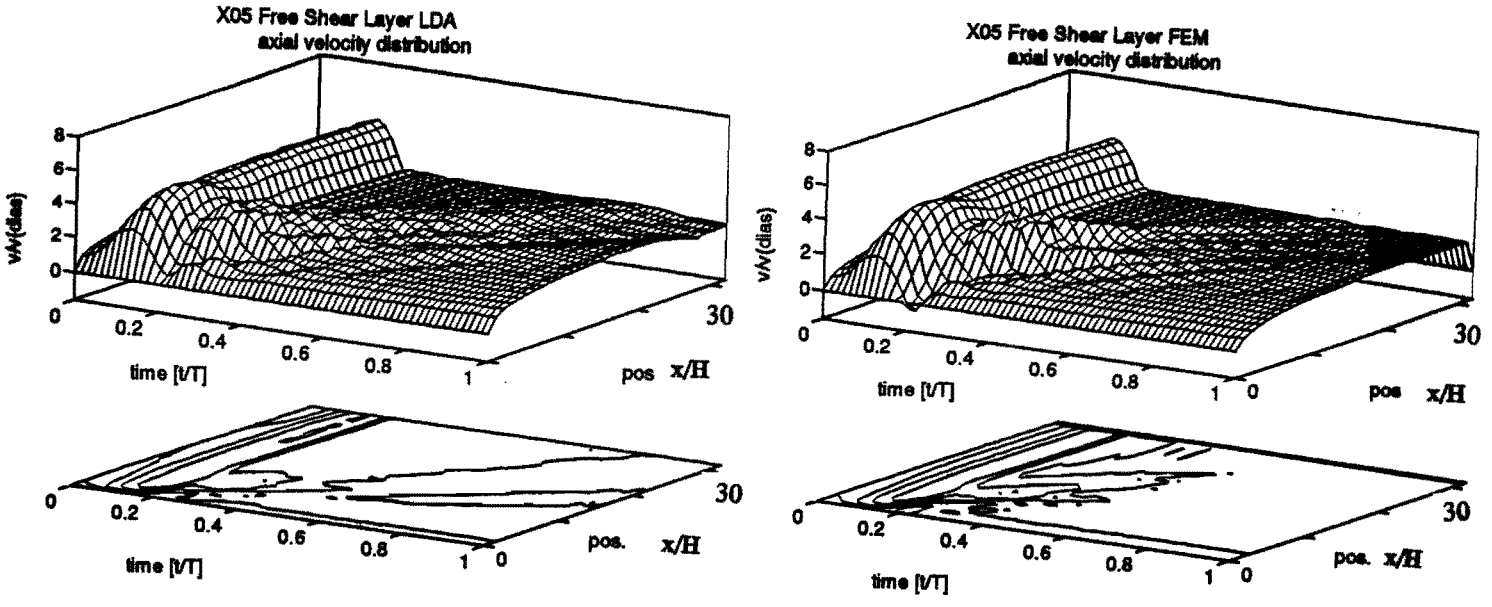

Figure 9. The axial velocities at site X05 as a function of time for the LDA measurements (left) and the FEM computations (right).

Conclusions and discussion

Experimental techniques and finite element computations on a free shear layer flow have been compared in this paper. It is seen that the finite element method used provide good approximations of the shear layer as the experimental and numerical results agree rather well. A more quantitative comparison between the LDA experiments and the FEM computations is given in figure 10. Here the axial velocities in a few points are plotted as a function of time for both the LDA experiments as the FEM computations. It can be seen that the velocity at the diastolic phase of the flow pulse is a little higher for the LDA measurements probably due to the fact that the experiments are made in a three dimensional fluid circuit. The velocity profiles will also develop in the third dimension. The Reynolds number has been based on the total experimental three-dimensional flow. The largest differences are seen at the decelerating part of the systole with the highest velocity gradient and near the oscillations. This might be due to the fact that there is a large difference between periods where the oscillations are present in the flow pulse (see figure 11). Here the mean velocity in a point is given as a function of time with its standard deviation for the LDA measurements. By the averaging over periods a loss in information of the oscillations occurs.

As is seen from the LDA measurements at site Y00 a small oscillation can already be seen before the two streams merge. It seems that there is a relation between this oscillation and the fact that the flow ratio is not constant over one period time of the flow pulse. It is assumed that a nonlinearity of the fluid circuit can be held responsible for the unsteadiness of the flow ratio and thus for the initial perturbation. If that is the case, the evolution of a forced perturbation has been studied. Finite element computations on the merging of two

perfectly parallel pulsatile flows show that the phenomena that have been observed are very sensitive to the inflow conditions (see figure 12). Different wavelengths and less vortices can be seen. This might be a confirmation of the assumption mentioned above.

In the experimental geometry used here a separation plate is involved with a length of approximately 110H (55 cm) and boundary layers are developed at this plate. The effect of these boundary layers and thus the effect of the developed inflow velocity profiles is still unknown. As it is known that vorticity is usually generated in boundary layers their existence might be of great influence for the generation of the perturbations in a free shear layer and therefore should be studied carefully.

This discussion leads to the question what kind of instability is observed in the experiments and computations. Still the perturbations do not seem to be caused by vortex shedding at the tip of the separation plate. After all four vortices have been generated in the shear layer simultaneously within 10H downstream of the tip of the separation plate.

From the results presented in this paper it can be concluded that the transient stability of a shear layer with flow ratio 1:3 occurs, for a pulsatile unsteady flow. The first instabilities can be observed within 10H (5 cm) of the tip during the decelerating phase of the systole with perturbation wavelength 1.6H (0.8 cm) and seem to grow linearly. Further downstream nonlinear growth can be seen as pairing of vortices occurs. The wavelength grows to 3.2H (1.6 cm) and 4H (2.0 cm). The vortices are moving with approximately the local velocity of the unperturbed flow. The presence of vortices with different wavelengths further downstream is assumed to be due to the fact that some vortices move with different velocity varying between 1.1 and 1.45 v(dias) (3.6 and 4.7 cm/sec). From this fact it can be concluded that spatial instability has been observed (Ho and Huerre, 1984).

The importance of this research is the relation with the flows through the carotid artery bifurcation, as there also occurs a free shear layer. Since perturbations observed here in the free shear layer are probably partly due to occurence of boundary layers at the separation plate the results can not directly be used for the shear layer in the carotid artery bifurcation. Besides, the flow in the carotid artery bifurcation is essentially three-dimensional. However further investigation on the influence of stenosis on the shear layer would possibly provide interesting information.

Finally it can be concluded that the FEM method is a rather good numerical method to simulate a free shear layer flow globally.

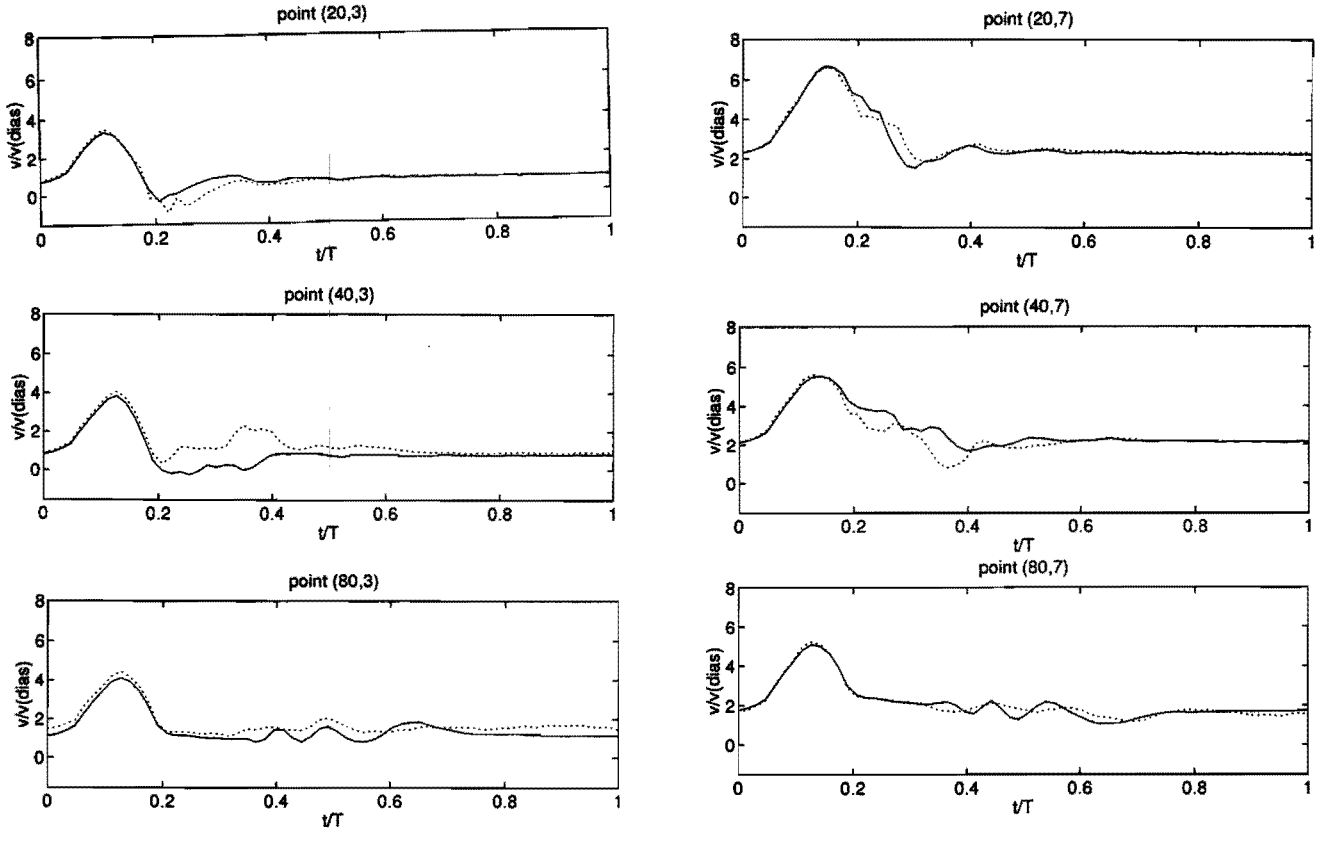

Figure 10. The axial velocities at a few points as a function of time for both LDA measurements (· · ·) and FEM computations (___).

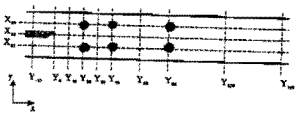

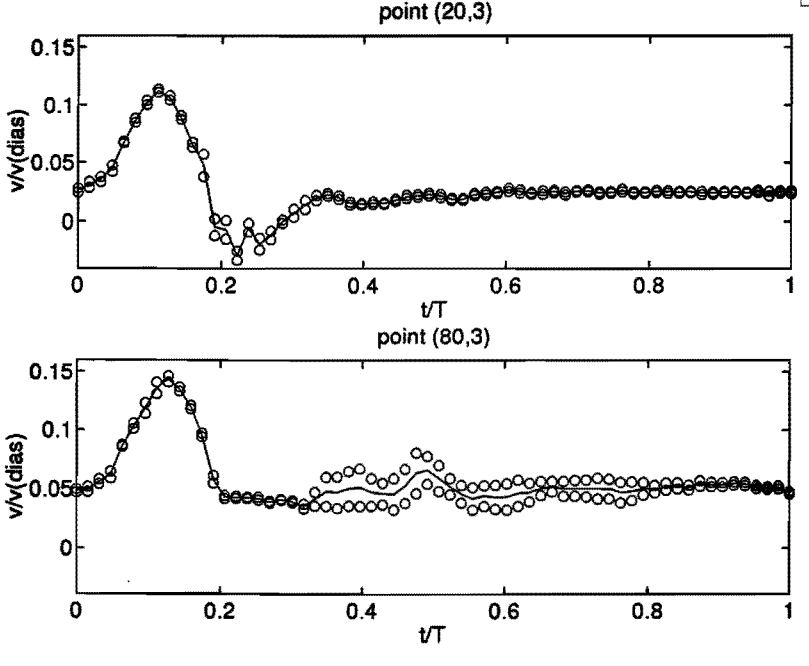

Figure 11. Mean velocity and standard deviation for two points for the LDA measurements.

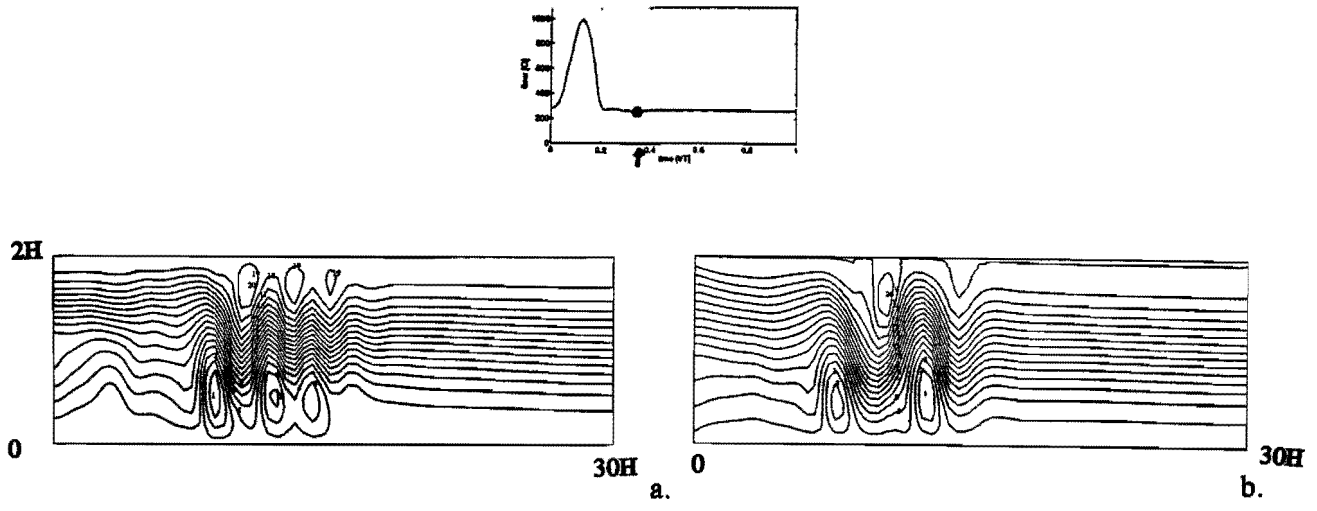

Figure 12. Comparison between FEM computations with the measured velocity profile at Y00 as inflow condition (a) and for perfectly parallel flows (b)

References

[1] Betchov and Szewczyk (1963) Stability of parallel flows. New York: Academic Press.

[2] Cuvelier et al. (1986) Finite element methods and Navier-Stokes equations. D. Reidel Publishing Comp. Dordrecht/Boston/Lancaster/Tokyo.

[3] Davis (1976) The stability of time-periodic flows. Ann. Rev. Fluid Mech., volume 8, 57-74.

[4] Drazin and Reid (1981) Hydrodynamic stability. Cambridge University Press.

[5] Esch (1957) The instability of a shear layer between two parallel streams. J. Fluid Mech. 3, 289-303.

[6] Gijsen (1993) The influence of a mild stenosis on the flow field in the carotid artery bifurcation. LDA experiments. WFW report 93-043

[7] Ho and Huerre (1984) Perturbed Free Shear Layers. Ann. Rev. Fluid Mech. 16, 365-424.

[8] Kelly (1965) The stability of an unsteady Kelvin-Helmholtz flow. J. Fluid Mech. 22, 547-560.

[9] Knio and Ghoniem (1990) Three-dimensional vortex simulation of roll-up and entrainment in a shear layer. J. Comp. Phys. 1990, 172-.

[10] Lie and Riahi (1988) Numerical solution of the Orr-Sommerfeld equation for mixing layers. Int. J. Engng Sci 26, 2, 163-174.

[11] Michalke (1964) On the inviscid instability of the hyperbolic-tangent velocity profile. J. Fluid Mech. 19, 543-556.

[12] Michalke (1965) On spatially growing disturbances in an inviscid shear layer. J. Fluid Mech. 23, 521-544.

[13] Miksad (1972) Experiments on the nonlinear stages of free-shear-layer transition. J.

Fluid Mech. 56, 695-719.
[14] Palmen, v.d. Vosse, Janssen and v. Dongen (1992) The influence of minaor stenoses on the flow in the carotid artery bifurcation. Submitted to J. Biomechanics.
[15] Rindt, v. Steenhoven, Janssen, Reneman and Segal (1990) A numerical analysis of steady flow in a three dimensional model of the carotid artery bifurcation. J. Biomechanics 23, 461-473.
[16] V.d. Vosse (1986) Numerical analysis of carotid artery flow. Phd Thesis, Eindhoven University of Technology.

Experimental and numerical analysis of an unsteady pulsatile free shear layer

Carla Reijnierse

Contents

APPENDIX A LITERATURE SURVEY

Research on the influence of mild stenosis on the flow in the carotid artery bifurcation shows that this flow is essentially instationary and three-dimensional. The flow can be characterized by a region of high shear and velocity along the divider wall and a separation zone with low velocity at the non-divider wall, see figure 1.

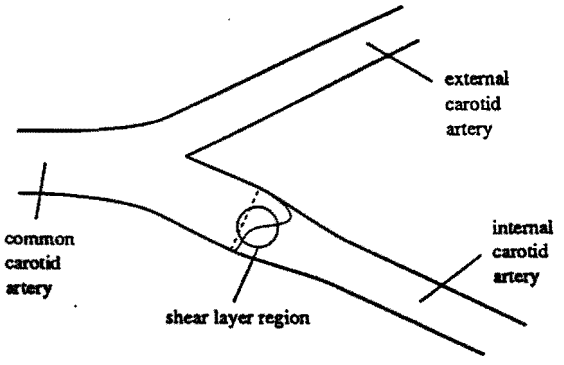

Figure 1. A typical velocity profile in the carotid artery bifurcation.

The interface between the two flow regions may be considered as a time dependent free shear layer. It is now expected (Palmen et al., 1992; Rindt et al., 1990) that this shear layer might be more sensitive to the existence of mild stenosis than other features of the flow field. It is assumed that the hydrodynamic stabilities of the free shear layer play an important role in the overall flow phenomena that occur in these kinds of bifurcation geometries. For this reason a literature survey has been done on flow instabilities of a simplified two-dimensional free shear layer.

A1. The theory of hydrodynamic stability of parallel flows

A1.1. Introduction

The theory of hydrodynamic stability deals with the question whether and how laminar flows become unstable. In this chapter only the stability of parallel incompressible flows is discussed. A commonly valid method to study instability is considering the evolution of the kinetic energy of a perturbation. For perturbations with small amplitude a linear theory will be discussed shortly in section A1.3 (Vossers,1980; Drazin & Reid, 1981). Finally an outline of a nonlinear theory is given in section A1.4.

A1.2. Definition of hydrodynamic stability

Consider area $\Omega(t)$ with boundary $\Gamma(t)$, moving with the fluid and assume a basic flow in an incompressible viscous medium with velocity $\mathbf{v}$ and a perturbed flow $\mathbf{v}^*$. The disturbance is now defined as $\mathbf{u} \equiv \mathbf{v}^* - \mathbf{v}$. Since the perturbed flow has to satisfy the same boundary conditions as the basic flow, the disturbances at the boundary equals zero. Looking at the way the kinetic energy of the perturbation evolves:

$$\varepsilon(t) = \frac{1}{2}\rho \int_{\Omega(t)} u^2 dV \tag{1}$$

a definition of hydrodynamic stability can be given. The flow is stable as long as $d\varepsilon/dt \leq 0$ and is unstable when the kinetic energy of the disturbances grows ($d\varepsilon/dt > 0$). By application of the Navier-Stokes equations for $\mathbf{v}$ and $\mathbf{v}^*$ the following equation can be obtained (Vossers, 1980):

$$\frac{d\varepsilon}{dt} = \frac{d}{dt}\frac{1}{2}\rho \int_{\Omega(t)} \vec{u}^2 dV = \rho \int_{\Omega(t)} (\vec{u}, \frac{d\vec{u}}{dt}) dV = \rho \int_{\Omega(t)} (\vec{u}, \nabla\vec{u}, \vec{v}) dV - \eta \int_{\Omega(t)} (\nabla\vec{u} : \nabla\vec{u}) dV \tag{2}$$

where η is the dynamic viscosity. The first term at the right-hand side represents the energy transfer from the basic flow to the perturbation. The second term is a dissipation term determined by the viscosity and is always negative and therefore will always stabilize the flow. When however the first term is larger than the dissipation term the perturbation is unstable. It shall always be possible to find a sufficiently high velocity and velocity gradient for instability to occur (Serrin, 1959).

A1.3. Linear theory of hydrodynamic stability

As mentioned before the theory of hydrodynamic stability deals with the question whether and how instability occurs in laminary flows. The equation describing the linear stability of parallel flows is known as the Orr-Sommerfeld equation. The Orr-Sommerfeld equation can be derived by assuming a parallel flow U(y) with small disturbances $u'(x,y,t)$ and $v'(x,y,t)$ parallel to and perpendicular to U. The linearized Navier-Stokes equations written in a form using the streamfunction of the disturbance defined by:

$$u' = \frac{\partial\psi}{\partial y} \quad and \quad v' = -\frac{\partial\psi}{\partial x} \tag{3}$$

written as an harmonic perturbation:

$$\psi(x,y,t) = \phi(y)\exp[i\alpha(x-ct)] \tag{4}$$

This gives the Orr-Sommerfeld equation written in dimensionless form (Drazin & Reid, 1981):

$$(U-c)\left(\frac{\partial^2\phi}{\partial y^2} - \alpha^2\phi\right) - \frac{\partial^2 U}{\partial y^2}\phi = \frac{1}{i\alpha Re}\left(\frac{\partial^4\phi}{\partial y^4} - 2\alpha^2\frac{\partial^2\phi}{\partial y^2} + \alpha^4\phi\right) \tag{5}$$

where Reynolds number Re is defined as VL/ν with V the averaged velocity, L a characteristic length and ν the kinematic viscosity. Solving this equation analytically will

give difficulties as both the wavenumber α and propagation velocity c of the perturbation can be complex numbers. Usually a distinction is made between temporal and spatial instability.

For temporal instability the wavenumber α is considered to be real and $\alpha>0$ and the propagation velocity $c=c_1+ic_2$ is complex. The perturbation streamfunction is now:

$$\psi(x,y,t) = \phi(y)\exp[i\alpha(x-c_1t)]\exp[\alpha c_2 t] \qquad (6)$$

The sign of c_2 determines whether the perturbation grows ($c_2>0$, unstable) or damps in time ($c_2<0$, stable).

For spatial instability both $\alpha=\alpha_1+i\alpha_2$ and $c=c_1+ic_2$ are complex, however $\alpha c=\omega$ is real. The perturbation streamfunction becomes:

$$\psi(x,y,t) = \phi(y)\exp[i\alpha_1(x-\omega t)]\exp[-\alpha_2 x] \qquad (7)$$

In this situation the sign of α_2 determines for the stability of the perturbation. When $\alpha_2>0$ the flow is called stable and for $\alpha_2<0$ there is instability.

Values for α, c_1 and c_2 respectively α_1, ω and α_2 can be obtained from the Orr-Sommerfeld equations as an eigenvalue problem in ϕ. It will be clear that the Reynolds number plays a crucial role in this eigenvalue problem. Stability curves can be found as given in figure 2. In figure 2a the amplification factor c_2 and phase velocity c_1 are presented as function of wavenumber α and the Reynolds number Re. The flow is unstable in the area where $c_2>0$. The situation in which $c_2=0$ is known as neutral stability. The phase velocity c_1 increases with Reynolds number at a fixed frequency. It can also be seen that at a fixed Reynoldsnumber the flow will be unstable only for a restricted frequency range. In figure 2b wavenumber α_1 and amplification factor α_2 are shown as a function of the frequency ω and Reynolds number Re. The flow is unstable in the area where $\alpha_2<0$. The stability curve for $\alpha_2=0$ is the neutral stability curve. For spatial instabilities there is also a restricted frequency range at a fixed Re.

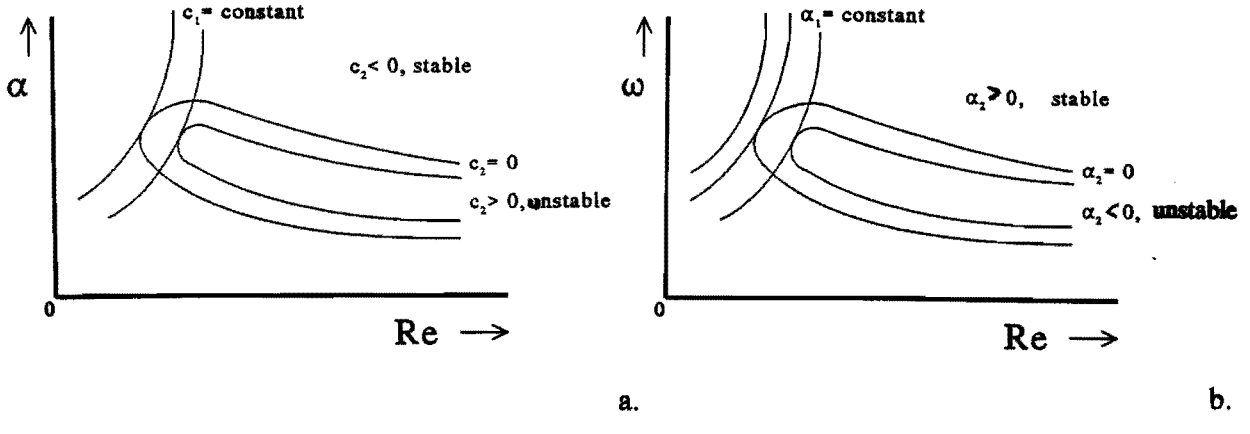

Figure 2. Temporal stability curves (a) and spatial stability curves (b)

In the limit of $Re\to\infty$ the Orr-Sommerfeld equation becomes in good approximation the

Rayleigh equation, which is far more easy to solve:

$$(U-c)\left(\frac{\partial^2\phi}{\partial y^2} - \alpha^2\phi\right) - \frac{\partial^2 U}{\partial y^2}\phi = 0 \qquad (8)$$

When solving this equation singularities occur in the areas where $U(y_c)-c=0$, the so called critical layer (Vossers, 1980). Therefore several approximation techniques are used to find solutions that are valid in this critical layer (Drazin & Reid, 1981).

An other very important reason to treat the viscous and inviscid situation separately, besides the complexity of the Orr-Sommerfeld equation, is that different mechanisms can be responsible for the occurence of instability. In the inviscid situation the responsible mechanisme is vortex induction. Here instability only occurs when the velocity profile has a point of inflection (Lin, 1955). Flows without a point of inflection can also be unstable. In this situation the role of viscosity is essential. Viscous forces are responsible for the production of a Reynolds stress, by which energy of the basic flow is transferred to the perturbation. The influence of viscosity can be bilateral. Viscosity can also be the cause of the damping of perturbations in case of flows having velocity profiles with points of inflection.

Experiments have shown that in most cases the linear theory is not sufficient (Ho & Huerre, 1984). A nonlinear theory should be used whenever the amplitudes of linear instabilities become to large to satisfy the condition of infinitesimal perturbations. An other important reason to use a nonlinear theory is the existence of essentially nonlinear instability.

A1.4. Nonlinear theory of hydrodynamic stability

Nonlinear theories are often based on the linear approximation as a starting point. Then nonlinear terms are taken into account and the development in time is calculated. Stuart (1960) made the restriction to small deviations of the neutral stable situation in the region with highest probability of instability in the vicinity of Re_c and α_c. Higher harmonics are taken into account in the perturbation streamfunction.

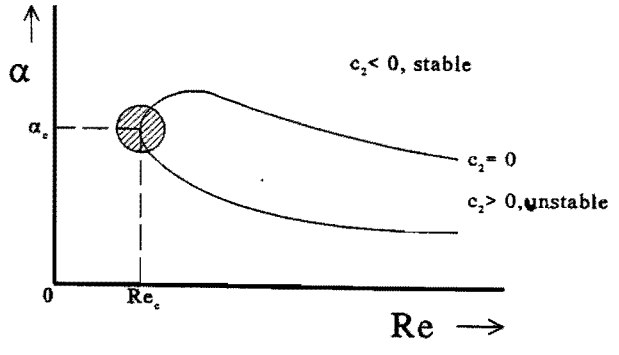

Figure 3. **The neutral stability curve, with ///: region investigated by Stuart.**

Stuart (1960) has derived an equation for the development in time of the amplitude A of the perturbation wave:

$$\frac{d|A|^2}{dt} = 2\alpha_c c_2 |A|^2 - 2\alpha_c k_2 |A|^4 \qquad (9)$$

This equation forms the basis of nonlinear analysis. For $c_2/k_2 < 0$ the nonlinear terms amplify the behaviour of the linear analysis. If $c_2/k_2 > 0$ periodic stable solutions are found. In this case ($c_2/k_2 > 0$) for $c_2 > 0$ unstable perturbations tend to reach a limit value $|A|^2 = c_2/k_2$. This is called an supercritical equilibrium. For $c_2 < 0$ a subcritical equilibrium is reached. If $|A|^2 < c_2/k_2$ stability occurs and if $|A|^2 > c_2/k_2$ instability occurs.

A2. The free shear layer

A2.1. Introduction

In this section the previous described theories will be applied on a free shear layer. A free shear layer is formed by the merging of two parallel streams initially separated by a thin surface. The flow is schematically drawn in figure 4.

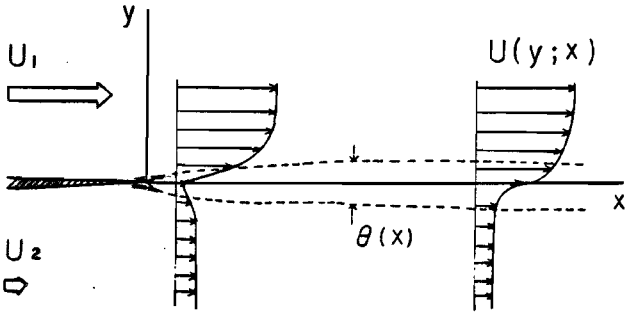

Figure 4. Spatially developing free shear layer, with Θ(x) the momentum thickness (Ho and Huerre, 1984)

In general two parallel laminar flows with velocity U_1 and U_2 ($U_1 > U_2$) are considered, giving rise to a weakly diverging basic flow U(x,y) because of viscous diffusion. Downstream the tip of the separating surface a shear layer will develop with a momentum thickness Θ(x). The flow can conveniently be characterized by two dimensionless parameters, the velocity ratio R and the Reynolds number Re based on the initial momentum thickness Θ_0:

$$R \equiv \frac{\Delta U}{2\overline{U}} \quad with \quad \Delta U = U_1 - U_2 \quad and \quad \overline{U} = \frac{1}{2}(U_1 + U_2) \qquad (10)$$

$$Re \equiv \frac{\overline{U}\Theta_0}{\nu} \tag{11}$$

The basic flow is now described by the hyperbolic tangent velocity profile:

$$U(y,R) = \overline{U}(1+R)\tanh(\frac{y}{2\Theta}) \tag{12}$$

If the basic flow is taken to be strictly parallel and perturbations are infinitesimal, the perturbation stream function can be cast into the form (section A1):

$$\psi(x,y,t) = \phi(y)\exp[i\alpha(x-ct)] + c.c. \tag{13}$$

Knio & Ghoniem (1990) have concluded that the development of two-dimensional shear layer instability can often be split into three regimes:

* The first regime is linear regime with linear growth. The amplitude of the perturbation grows exponentially and the form of the perturbation remains unchanged.
* In the second regime nonlinear growth occurs, characterized by roll-up and spreading of the shear layer in y-direction.
* In the third regime a completion of the growth of instability takes place, accompanied by pairing of vortex structures. Finally a transition to turbulence takes place.

In this section attention will be paid mainly to a homogeneous incompressible two-dimensional shear layer. In the first section a linear analysis will be presented. As this analysis is far from a complete description of a perturbed shear layer, a nonlinear theory is discussed in section A2.3. Finally in section A2.4 the development of vortex structures in the shear layer is described.

A2.2. The linear regime

The linear theory of hydrodynamic stability has shown to describe the initial development of a shear layer very satisfactory. Esch (1957) has shown that the inviscid theory yields very good results for $\alpha Re > 100$. He has studied a piecewise linear velocity profile, of which the results are quantitatively useful for a hyperbolic tangent velocity profile for small wavenumber α of the perturbation. For large values of α the results are only qualitatively correct. He compared numerical results obtained by solving the Orr-Sommerfeld equation with analytical results based on the Orr-Sommerfeld equation and on the inviscid Rayleigh equation. This comparison has led to the conclusion formulated above. The inviscid theory provides a good description of the perturbed free shear layer for $\alpha Re > 100$. Therefore in this section attention will be paid first to the inviscid theory

and afterwards to the viscous theory.

A2.2.1. The inviscid situation

In 1964 Michalke has determined numerically the characteristics of temporal waves in the inviscid limit Re $\rightarrow \infty$, using the Rayleigh equation. The calculations have been made for the unbounded hyperbolic tangent velocity profile:

$$U(y) = \frac{1}{2}(1+\tanh(y)) \tag{14}$$

Thus in the limit R=1, where only one stream is present.

It can be shown that because of symmetry the propagation velocity of the perturbation c_1 is independent of the wavenumber α for temporal instabilities: c_1=U(0)=0.5. The perturbations are moving with local velocity. In figure 5 the computed growth rate αc_2 and the amplification factor c_2 are given as a function of wavenumber α.

For spatial instability Michalke (1965) has made the same sort of computations. The results are shown in figure 5. Since only disturbances travelling and growing in basic flow direction are considered a restriction is made to values $0<\alpha_1<1$, $\alpha_2<0$ and $0<\omega<0.5$ (Michalke 1965).

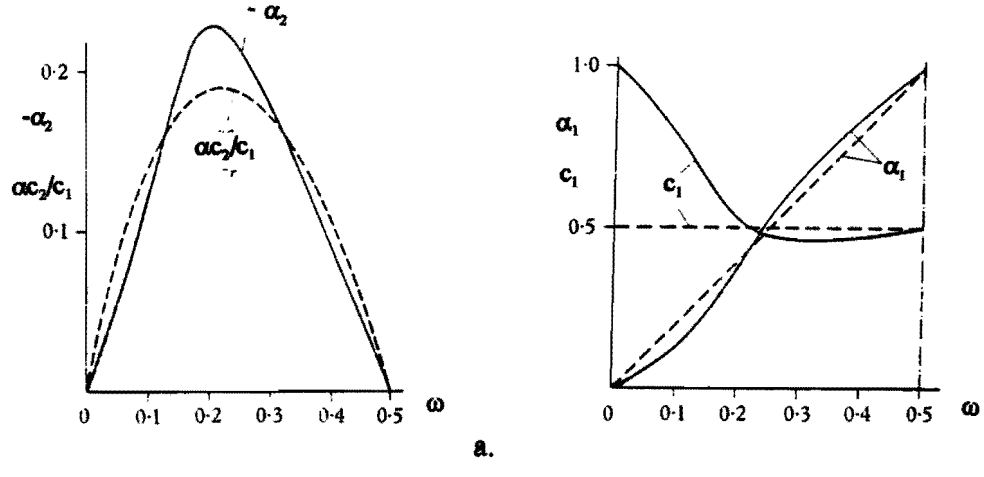

Figure 5. Spatial growth rate $-\alpha_2$ and αc_2 (a) and wavenumber α_1 and phase velocity c_1 (b) versus frequency ω. ——— :spatial; --- : temporal. (Michalke, 1965)

In contradiction to the temporal case, the phase velocity c_1 for spatial instabilities depends strongly on the frequency especially for small frequencies. Whereas for temporal instabilities the phase velocity is a constant. This behaviour has also been observed in experiments within a large range of values of ω.

Ho & Huerre (1984) have studied the non-dimensional spatial growth $\alpha_2\Theta/R$ as function of

the Strouhal number for different values of velocity ratio R. The Strouhal number is defined as:

$$St = \frac{f\Theta}{U} \qquad with\ f = \frac{\omega}{2\pi} \tag{15}$$

These calculations show that the maximum spatial growth rate $(\alpha_2\Theta)_{max}$ increases approximately linear with velocity ratio R, see figure 6a. The Strouhal number $St_n = 0.032$ of the most amplified wave corresponds to the natural frequency of the shear layer. It changes only 5% between R=0 and R=1. The phase velocity c_1 associated with the natural perturbation is equal to the average velocity of the two streams, see figure 6b. Again it shows that the perturbation moves with local velocity. Waves with a frequency different from the natural frequency move with a velocity different from the mean velocity.

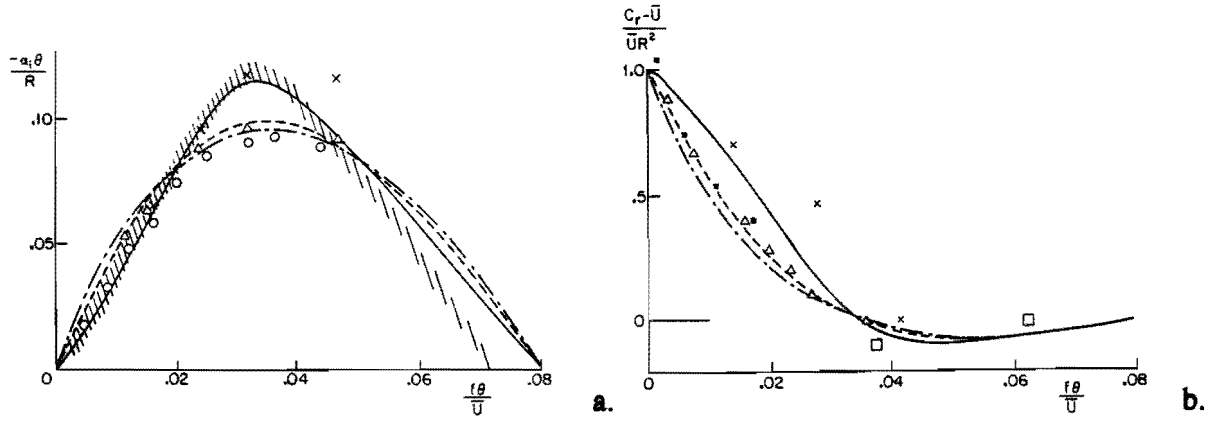

Figure 6. Variations with R of (a) the normalized amplification rate $-\alpha_2\Theta/R$ and (b) the normalized phase velocity $(c_1-\bar{U})/\bar{U}R^2$ as a function of the Strouhal number. Calculations:__ : R=0; _.._ : R=0.5 ; --- : R<<1. Experiments: □:R=1 (Sato 1960); ○:R=1 (Freymuth 1966); ×:R=0.72 (Miksad 1972); \\\:R=1 (Fiedler et al. 1981); △:R=0.31 (Ho & Huang 1982); ■:R=1 (Drubka 1981) (Ho and Huerre, 1984)

From figure 6b it is also noted that in contrast with temporal waves spatial waves are dispersive below St_n and non-dispersive above.

The discussion above is based on unforced shear layers. In most cases however, the flow is forced at a specific frequency f_f with a perturbation such that the amplitude of the perturbation is relatively small and within the linearly unstable range. Figure 7 summarizes the response of a shear layer to an excitation f_f close to f_n. The variations of the main frequency components f_f and $f_f/2$ and the momentum thickness $\Theta(x)$ are represented along the streamwise direction. The peak of the power spectrum immediately downstream of the trailing edge is found to occur at the calculated natural frequency f_n. Beyond the region of exponential growth, Kelvin-Helmholtz instability waves develop into a periodic array of compact vortices moving at the average velocity with a wavelength $\lambda_n=\bar{U}/f_n$, see figure 8. The recirculating regions, which contain most of the vorticity, are usually referred to as

Kelvin Cat's eyes.

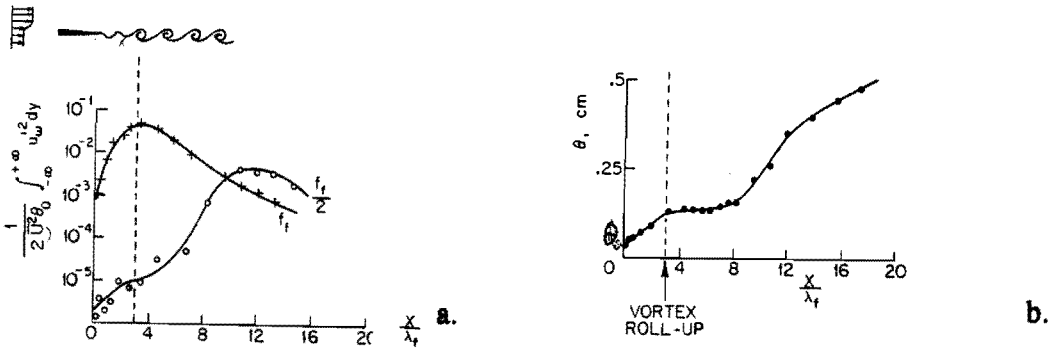

Figure 7. Evolution of (a) spectral components f_f and $f_f/2$ and (b) the momentum thickness with downstream distance x/λ_f. $f_f \approx f_n$. u_ω' is the narrow-band velocity fluctuation centered at ω. (Ho and Huerre, 1984)

Figure 8. Roll-up of vortices. $f_f \approx f_n$. R<1. (Ho and Huerre, 1984)

This so called roll-up proces is predominantly two-dimensional and is completed at the downstream station where the fundamental component at frequency f_n reaches its maximum amplitude, figure 7a. It is accompanied by the generation of a subharmonic component $f_n/2$. The linear stability theory may only approximately describe the exponential growth of the perturbation. A weakly non-linear theory might be appropriate to model the further evolution.

A2.2.2. The viscous situation

In this section the effect of viscosity on the stability of free shear layers is discussed. One has to keep in mind that already in the inviscid limit instability occurs. The existence of a point of inflection explains this, section A1.2. In such cases viscosity will mainly act as a damping mechanism (Vossers, 1980). Studies on viscous hyperbolic tangent velocity profile have been made by Esch (1957) and Betchov (1963) for temporal instabilities. The results are shown in figure 9. The dimensionless spatial growth $\alpha\Theta$ and amplification factor $c_r/\bar{U}$ are given as a function of Reynolds number Re.

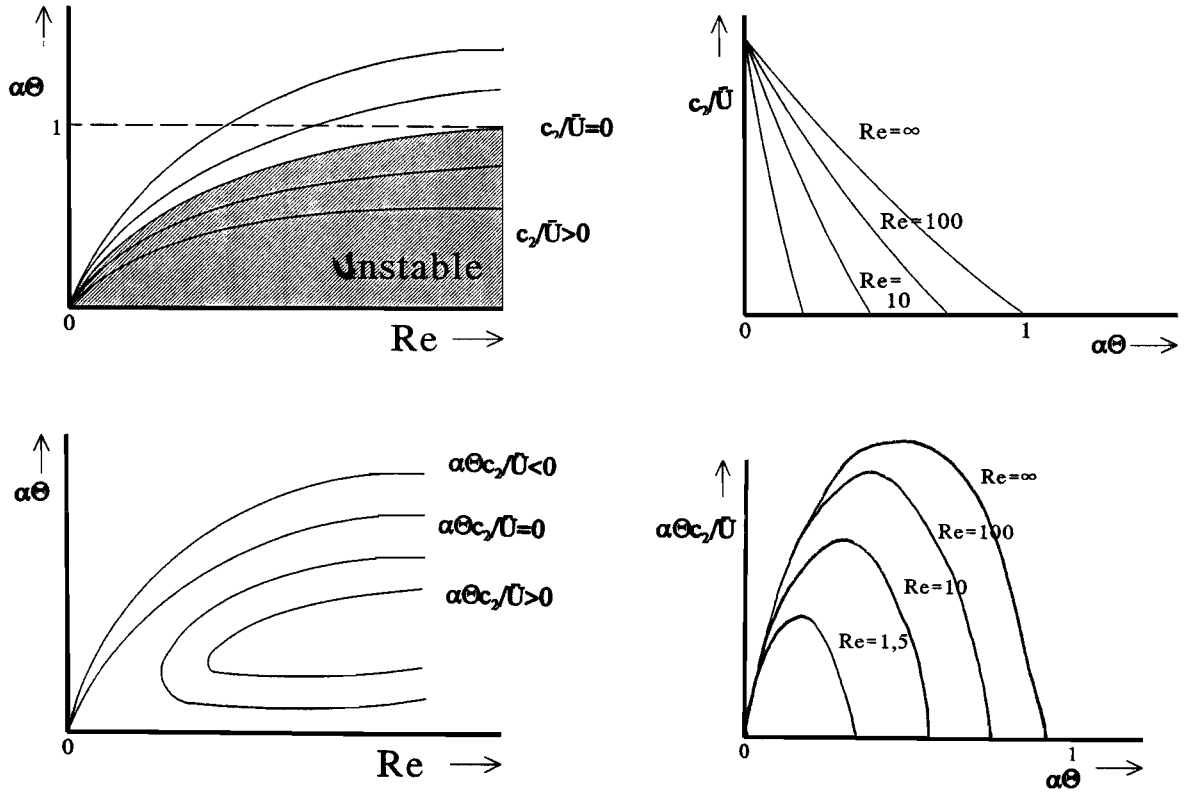

Figure 9. Theoretical results for a shear layer with a hyperbolic tangent velocity profile (Betchov, 1963; Vossers, 1980).

In the inviscid limit Re→∞ the results correspond with the results of Michalke (1965) in figure 5.

The instability regime diminishes for smaller Reynolds numbers. The figures show that in principle no minimum Reynolds number exists below which no instability occurs. However this conclusion is based on unbounded parallel flows. The presence of boundaries, which will always be there in experiments, is expected to result in the existence of a minimum Reynolds number. For the bounded geometry limits the perturbation wavelength and thus will result in a minimum wavenumber $\alpha>0$. The minimum Reynolds number shall occur where the neutral stability curve reaches that value of α.

Ho and Huerre claim that the calculated growth rates are rather insensitive to variations in the Reynolds number (based on the initial momentum thickness) for Re>50. In most experiments the initial Reynolds number will be 100 or more and viscosity will therefore not directly effect the roll-up and pairing of the vortices.

Calculations on spatial instabilities by Lie & Riahi (1988) have shown a low minimum Reynolds number for the unbounded flows. They also have shown that the viscous modes are more unstable than the inviscid modes. Viscous modes are the modes that do not exist in the inviscid limit Re→∞, while the inviscid modes correspond with those in the inviscid

limit. It was also seen that increasing viscosity results in damping of the instability.

A2.3. The nonlinear regime

As soon as the weakly amplified pertubation in a free shear layer reaches a certain size the influence of nonlinear terms become important. At this point subharmonic components are generated.

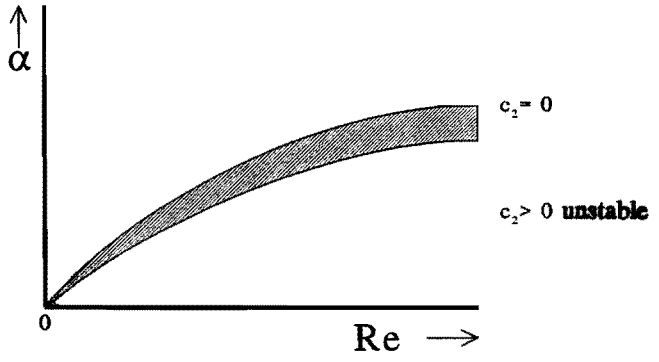

Figure 10. Linear stability curve

The nonlinear theory is often based on small deviations from the neutral stability curve, figure 10. In this region $c_2 > 0$. Calculations (Vossers, 1980; Maslowe, 1977) have shown that in a large range of parameters the supercritical equilibrium takes place with the complex perturbation amplitude A(x,t) defined as in section A1.4. The amplitude satisfies the Landau equation:

$$\frac{1}{A}\frac{dA}{dt} = a_0 + a_2|A|^2 \qquad (16)$$

with a_2 the Landau constant (this is a measure for k_2: $a_2<0$ then $k_2>0$) and a_0 can be identified with αc_2, as defined in section A1.4.

Maslowe (1977) has calculated the Landau constant for different Reynolds numbers and found $a_2 = -16/3\pi$ for $Re\rightarrow\infty$. In the unstable regime a stabilization to a finite amplitude $|A|^2_c=c_2/k_2$ takes place. These calculations are based on the Stuart theory and therefore based on small deviations from the neutral stability curve.

The nonlinear theory also describes the creation of Kelvin's Cats eyes in the layer, where the phase speed of the wave matches nearly the basic flow velocity. The balance between nonlinear effects and viscous dissipation in that layer can be characterized by a Reynolds number Re_{cl}. When $Re_{cl}>>1$ the amplitude A satisfies an equation admitting oscillatory solutions, the Kelvin's Cats eyes. These can be satisfactory modelled by the exact solution of the 2D-Euler equations with the associated streamfunction:

$$\psi(x,y,t) = \frac{Ua}{4\pi}[y + 2Rln\left(\cosh(\frac{2\pi y}{a}) - \rho\cos(\frac{2\pi}{a}(x-Ut))\right)] \tag{17}$$

where a is the distance between consecutive vortices and ρ a vorticity concentration parameter.

As mentioned at the beginning of this section a subharmonic component is generated downstream by pairing of vortices. Successive mergings of vortices is indeed the primary process governing the streamwise growth of the shear layer (the third regime). The pairing location occurs at the downstream station where the subharmonic reaches a maximum, figure 7. An analytical description of the vortex merging mechanism is not yet available. Ho & Huerre have considered the spatial nonlinear interaction of a fundamental wave with frequency f_n:

$$\psi_A(x,y,t) = A(x)\phi_A(\frac{y}{\theta(x)})\exp[-i\omega_n t - i\beta] + c.c. \tag{18}$$

and its harmonic $f_n/2$:

$$\psi_B(x,y,t) = B(x)\phi_B(\frac{y}{\theta(x)})\exp[-i\frac{\omega_n}{2}t] + c.c. \tag{19}$$

with a phase difference β between the two waves. Figure 11 shows that the greater the phase difference the smaller the subharmonic peak. The momentum thickness Θ(x) is growing slower for greater phase differences.

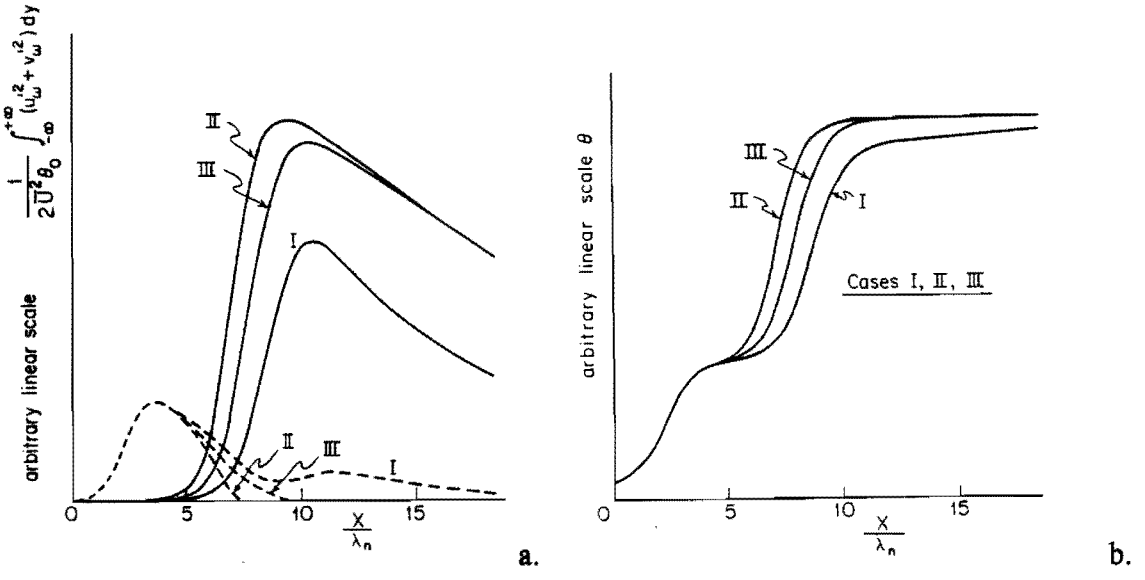

Figure 11. Evolution of the spectral components f_n (---) en $f_n/2$ (——) (a) and the momentum thickness Θ (b) versus downstream distance. The initial phase difference β is: (I): β=π; (II): β=0; (III): the two waves are uncoupled. R=0.31. (Ho and Huerre, 1984)

Direct computations of the vortex-pairing interaction in shear layers have been conducted by several people (Ho & Huerre, 1984). In all cases the flow was assumed to be spatially periodic and evolved in time. It was concluded from these computations that the smaller the initial phase difference the faster the coalescence of the two vortices. A pairing interaction is illustrated in figure 12 for three different initial phase differences.

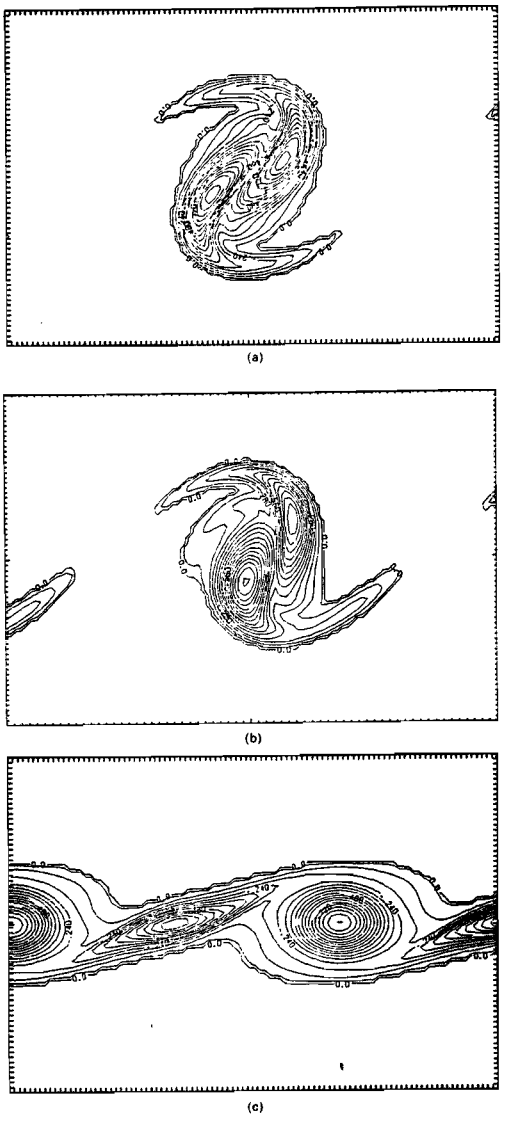

Figure 12. Interaction between the fundamental and subharmonic component in a temporally developing shear layer, using the numerical simulation of Riley & Metcalfe (1980). The initial phase difference is :(a) $\beta=0$. (b) $\beta=\pi/2$. (c) $\beta=\pi$. (Ho and Huerre, 1984)

A2.4. Vortex structures

Hydrodynamic instability can also be described with vortex structure dynamics. Mehta et al. (1987) showed that this method gives good results for the excitated shear layer and agrees both qualitative and quantitative with experiments. The Navier-Stokes equation nevertheless shows good results describing the whole evolution of the shear layer inclusive the effects near the trailing edge.

Spalart has used the vortex blob method to simulate a free shear layer. This method gives an approximation of the motion of a two-dimensional vortex-sheet by following the motion in time of a system of vortices with finite core, the so called vortex blobs. The vorticity is then defined by:

$$\omega(x,y,t)=\sum_{\alpha=1}^{N} \kappa_\alpha \gamma_\alpha(|x-x_\alpha(t)|,|y-y_\alpha(t)|) \tag{20}$$

where γ_α is the vorticity distribution within a vortex $x_\alpha = (x_{\alpha,y}\alpha)$ and κ_α the circulation of the vortex.

$$\int \gamma_\alpha(x,y)dxdy = 1 \tag{21}$$

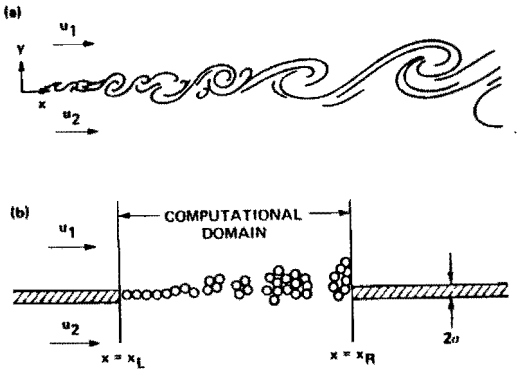

Figure 13. Schematic presentation of a 2D free shear layer (a) and a vortex simulation of a free shear layer (b). [Leonard 1980]

At each time step a new vortex with a gaussian core is placed at the edge on the lefthand side at $x=x_L$ and $y=0$. The circulation κ of each vortex is defined by Leonard (1980) and is such that at the edge the local flow conditions are satisfied:

$$\kappa = -\frac{\Delta t}{2}(u_1^2 - u_2^2) \tag{22}$$

In a non-perturbed shear layer vortices move with velocity $(u_1+u_2)/2$ and the normal distance between two vortices is $d= 2\Delta t/(u_1+u_2)$. The core size σ has to be of order d to achieve a fluent representation of the shear layer. Here σ=3d. The inflow condition is satisfied by the creation proces described above. The outflow condition is simply satisfied by removing the vortices reaching the boundary on the right $x=x_R$. Figure 14 presents the results achieved by Ashurst. Streakline plots are shown for two Reynolds numbers on successive time steps. The flow with highest velocity is the bottom flow. The pairing of vortices, present in experiments, is evidently clear.

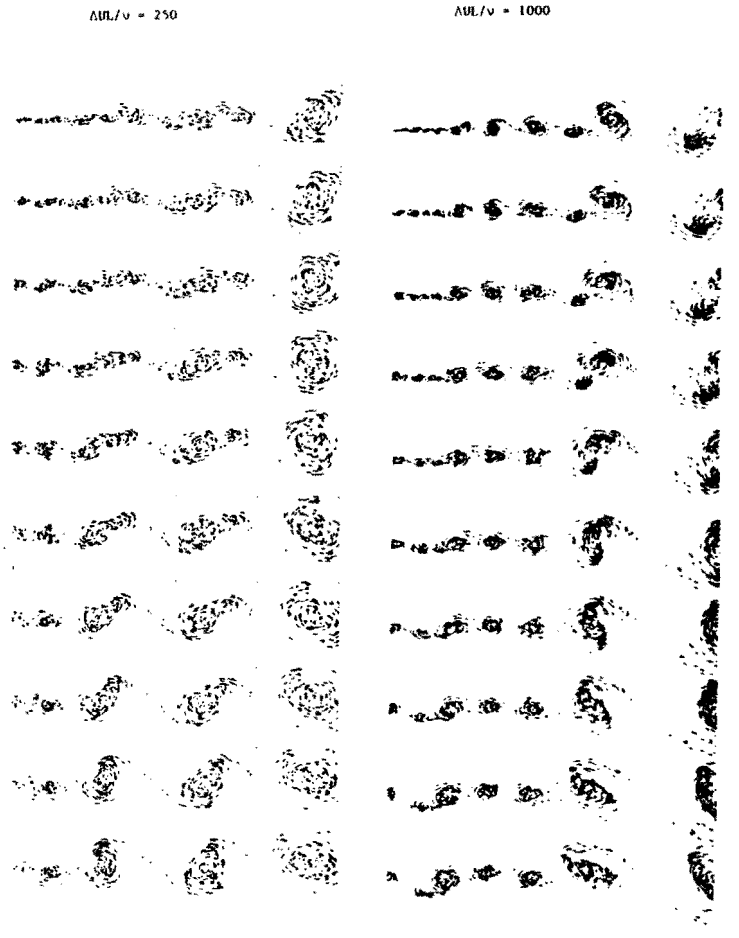

Figure 14. Streakline plots. Left column: Re=250. Right column: Re=1000. 1/R=2.1. (Leonard, 1980)

A3. Complicating factors

A3.1. Boundary effects

The preceding sections have dealt with unbounded two-dimensional steady free shear layers. In experiments however you never deal with perfect two-dimensional flows and experimental flows will always be bounded. For this reason a short discussion is given on these complicating factors.

The presence of boundaries has a damping effect on the development of instabilities. Esch (1957) has already mentioned that when temporal stability analysis is applied on a piecewise linear unbounded velocity profile, see section A2.2.2. There was no minimum Reynolds number noticed, below which no instability occured. This however was unlike the expectations, based on previous research by Lin on a boundary layer at a flat plate where a minimum Reynolds number was observed. Esch expected that the presence of boundaries would have resulted in observing a minimum Reynolds number for the free shear layer as well. After all a bounded geometry suggests a maximum perturbation wavelength and therefore a minimum value of wavenumber α. Thus a minimum Reynolds number has to exist corresponding with that value of α.

Lie et al. (1988) have studied the influence of boundaries on the stability of free shear layer with the help of spatial analysis. They have found a very small minimum Reynolds number for the unbounded situation. The presence of boundaries was seen to result in a much higher value of the minimum Reynolds number. These results are summarized in figure 15 where the velocity ratio R is given as a function of the minimum Reynolds number Re where instabilities occur.

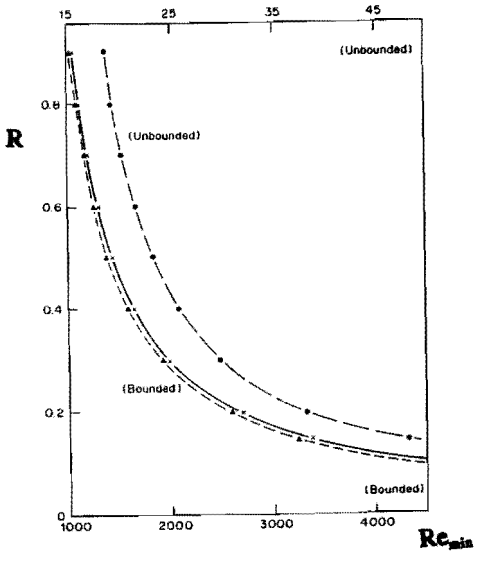

Figure 15. Minimum Re for bounded (lower axis) and unbounded (upper axis) flows as function of the velocity ratio R. _._:spectral method, unbounded; ___:spectral method, bounded; ---:Galerkins method, bounded
(Lie et al., 1988)

A3.2. Three-dimensional effects

The importance of three-dimensional effects was first mentioned by Miksad (1972). Studying the evolution of instabilities in a free shear layer he noticed that there is first an exponential growth of the fundamental perturbation, obeying the linear theory. Next subharmonic and harmonic modes arise and nonlinear growth takes place. Finally three-dimensional deformations of the fundamental mode appear resulting in a secondary vortex structure, after which a definite transition to turbulence takes place, where 3D activity dominates the flow.

Three-dimensional deformations of the basic flow and the fluctuating components are caused by the occurence of so called spanwise vortices and coincide with a decrease of energy of the fundamental mode. The initial wavelength of the spanwise perturbations agree with the wavelength of the fundamental mode. Increasing of three-dimensional activity results in a decrease of that wavelength (Miksad, 1972).

The occurence of three-dimensional activity is thought to be due to the presence of side walls. Probably waves are generated by the boundary layers at these walls. The generated waves will spread in the form of spiral threads along the axis of the spanwise structures. Once the secondary structure has been formed a transition to turbulence takes place and results in complete internal mixing (Miksad,1972).

A3.3. Unsteady periodic flows

As this project is merely an experimental and numerical research on unsteady periodic free shear layers this section presents a discussion on the stability of unsteady periodic flows. Stability of unsteady flows is a relatively new and unstudied subject within the theory of hydrodynamic stability. A mathematical analysis is far more complex as normal mode analysis is not applicable any more. Because of the time dependence of the basic flow the exponential time dependence is not separable. Even the meaning of stability is not completely clear when the magnitude of the basic flow changes substantially with time. In this section only the basic flows that are periodic in time, parametric instability, will be discussed. As the flow is periodically unsteady it seems natural to compare the growth rate of the perturbation with variations of the basic flow.

A periodic flow is called unstable whenever a perturbation experiences a net growth over every period of the basic flow. The situation in which every perturbation is damped on each moment is a monotonically stable situation. It is also possible that the perturbation will only grow during part of the cycle, reaches a maximum amplitude and will be damped next. This is called transient stability (Davis, 1976).

Considering the free oscillations of perturbations of the time averaged basic flow, the essential mechanism of parametric instability is a resonance between the forced oscillation of the basic flow and the free oscillation when the frequency of a free oscillation is half or an integral multiple of the frequency of the forced oscillation. The detailed properties of parametric instability may be exploited to create instability or stability by controlling the frequency and amplitude of the forced oscillation of the basic flow (Drazin and Reid, 1981).

Kelly (1965) showed in his article that when a free shear layer consists of two parallel unsteady streams with different densities, the oscillations of the basic flow can cause a subharmonic resonance such that a wave, which is neutrally stable in the absence of the oscillations and whose frequency is half of the frequency of the flow oscillations, becomes unstable.

4. Discussion

The findings in this literature survey give rise to some expectations in relation to the experiments on shear flow instability. In stationary situations with velocity difference $\Delta U \neq 0$ and sufficiently high Reynolds number a perturbation with natural frequency will grow exponentially, according to the linear theory, after which a nonlinear growth will take place in the form of roll-up and spreading of the shear layer. Pairing of vortices corresponds with the generation of a subharmonic component. Finally a transition to turbulence will occur (Knio and Ghoniem, 1990). For low Reynolds numbers perturbations will be damped. In the experiments that have been done during this study the Reynolds number is that low that no transition to turbulence is expected. Therefore three-dimensional effects do not have to be taken into account (Miksad, 1972).

From this literature survey it can also be concluded that viscosity and the presence of boundaries both have a damping effect on the instabilities of a flow (Esch, 1957; Betchov, 1963; Lie et al., 1988).

In unsteady flows three situations can arise (Davis, 1976):

* First a periodic flow is called unstable whenever a perturbation experiences a net growth over every period of the basic flow.
* The situation in which every perturbation is damped on each moment is a monotonically stable situation.
* Transient stability occurs when a perturbation will only grow during part of the cycle, reaches a maximum amplitude and will be damped next.

APPENDIX B. THE EXPERIMENTAL SETUP

In this appendix the experimental setup, used for the visualization and Laser Doppler Anemometry (LDA) experiments performed for this study are discussed. In the first section the experimental fluid circuit and the realization of the flow pulse are discussed. In the second section the two experimental methods, dye visualization and LDA, are presented.

B1. The experimental circuit

The experimental circuit used to study the shear layer instability is schematically represented in figure 1.

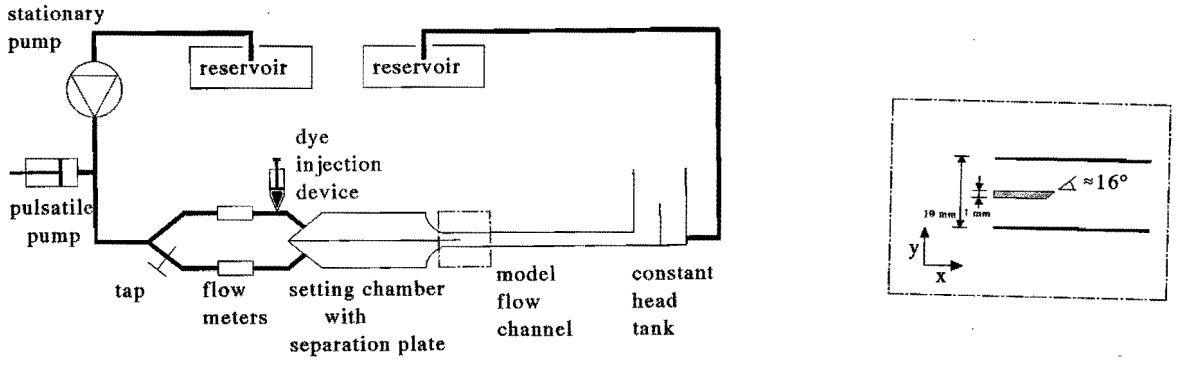

Figure 1. The experimental circuit.

The fluid used is water at room temparure and is pumped from a reservoir by an stationary pump. The flow is separated and led into the settling chamber. In the settling chamber the two streams are kept separated by a thin surface in the middle of the chamber. The height of the flow channel is 2H, where H=0.5 cm and the width of the channel is 12H. The thickness of the separation plate is H/5. The tip of the separation plate is also presented in figure 1 and has an angle of 16°. Before the upper flow enters the settling chamber dye can, if necessary, be injected by an injection device. Leaving the settling chamber the two streams merge in the flow channel and a so called free shear layer is formed. Two flow sensors are connected on the inlet tubes in front of the settling chamber. At the end of the flow channel the fluid is led into a reservoir again. The flow ratio can be controlled by a tap on the inlet tube of the bottom flow. By means of a computer controlled pulsatile pump connected downstream the stationary pump, a pulsatile flow can be generated.

The flow sensors used are electromagnetic flow probes. Therefore NaCl has to be added to the water. The signal from the flow probe is send to an adaptor and subsequently to a control unit. The result is a signal in volts, linearly dependent on the flow to be measured. An amplified signal is send to a computer controlled measuring unit and stored.

The flow pulse used is a modelled physiological pulse as shown in figure 2. The dimensionless parameters describing this flow pulse are the Reynolds number Re and the

parameter of Womersley α, based upon the flow conditions in the common carotid artery.

$$Re = \frac{2HU}{\nu} \tag{1}$$

$$\alpha = \frac{2H}{2}\sqrt{\frac{\omega}{\nu}} \tag{2}$$

where U is the mean velocity in the flow channel, 2H the height of the channel, υ the kinematic viscosity of the fluid and $\omega=2\pi/T$ the angular frequency with T=4.33 s the period time of the flow pulse.

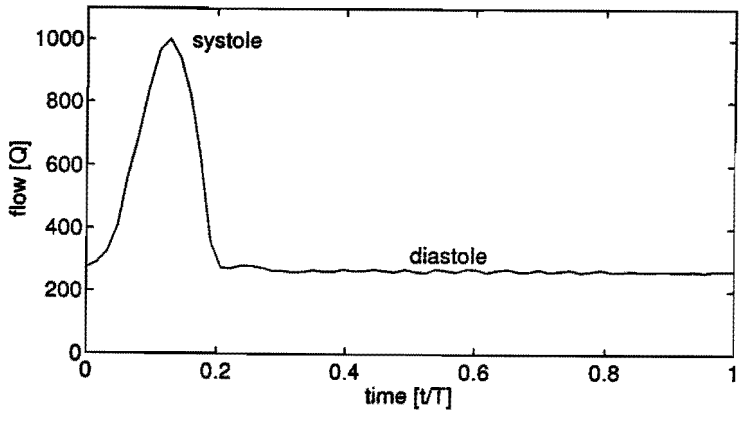

Figure 2. **Flow pulse.**

The flow ratio between the bottom flow Q_2 and upper flow Q_1 is 1:3, chosen for its similarity with the physiological situation.

The stationary pump used is a gear pump, which output flow can be varied continuously. The pulsatile pump generating the systolic peak of the flow pulse, is a piston pump with a cylinder of glass and a nylon piston. The piston pump is controlled by a servo amplifier unit. A position curve, generated in a MATLAB program is send to the amplifier by an ASYST program. As the systolic peak of the modelled flow can be represented by a cosine and the diastolic phase is a stationary component, the theoretical position curve has to be a superposition of half a cosine and a straight line. Previous investigations (Snijders 1992) however showed that to compensate the backlash of the piston ring a steplike function had to be inserted at the end of the cosine motion of the piston, see figure 3.

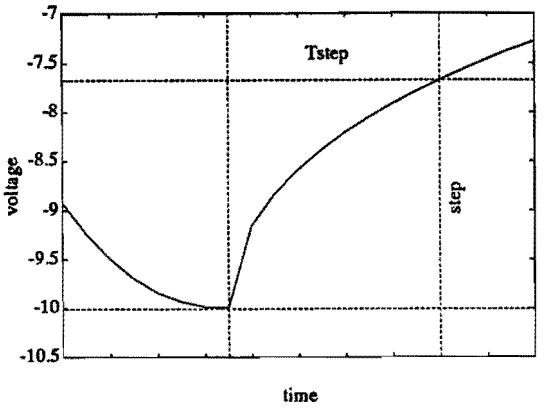

Figure 3. **Applied position curve for piston pump.**

B2. Experimental methods

B2.1. Dye visualization

To visualize the flow patterns of a free shear layer a dye visualization method has been used. Fluorescent dye has been injected by the injection device, see figure 1. The dye has been injected in the upper flow with highest velocity. It is important that the dye is of the same density as the fluid, so gravity influences may be neglected. This has been achieved by diluting dye with circuit water and by adding a few drops of alcohol. Before the merging of the the streams, thus before reaching the edge of the separation plate, the fluorescent dye has completely mixed with the fluid of the upper flow. This way the shear layer is clearly visualized and the flow phenomena in the shear layer are clearly visible.

B2.2. Laser Doppler Anemometry (LDA), the back scatter principle

Quantitative velocity measurements are made with the help of Laser Doppler Anemometry. LDA is the measurement of fluid velocities by detecting the Doppler frequency shift of laser light that has been scattered by small particles moving with the fluid. This technique offers numerous advantages: it is non-intrusive, it allows the unambiguous measurement of one or more components of the velocity vector, there is a linear connection between velocity and Doppler frequency, it offers reasonably good spatial resolution and the small measuring volume in combination with the fast electronics makes measurements on highly fluctuating flows possible. A disadvantage is that this method requires the presence of sufficient small particles often resulting in the need to add seeding. As this is an optical method the fluid and its environment has to be transparent.

The fundamental phenomenon in LDA is the Doppler frequency shift of scattered light from small moving particles (Goldstein, 1983). The usual situation is shown in figure 4, where the particle located at x(t) scatters the light wave with complex electric field vector $\mathbf{E}_{pl}$ from an incident illuminating beam $\mathbf{E}_{0l}$. The illuminating beam may be assumed to be a plane wave, linearly polarized in the spatial region where it illuminates the particle. Its frequency is ω_{0l}, its direction of propagation is $\mathbf{s}_l$, its wavenumber is $k=2\pi/\lambda$, its direction of linear polarization is $\mathbf{p}_l$, and its intensity is I_{0l} (W/m^2).

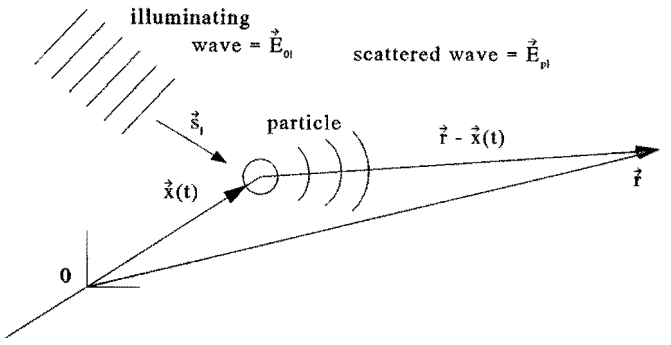

Figure 4. Light scattered by a moving particle.

It may be represented by the complex wave:

$$\vec{E}_{0l} = \sqrt{I_{0l}(x)}\exp[i(\omega_{0l}t - k\vec{s}_l\cdot\vec{x}]\vec{p}_l \tag{3}$$

The particle scatters a light wave from $\mathbf{E}_{0l}$ in all directions, and a point **r** is said to be in the far field of the particle if the distance r is much greater than both the wavelength of the light and the mean diameter of the particle. In the far field the scattered light is a spherical wave, regardless of the particle's shape, given by:

$$\vec{E}_{pl} = \sqrt{I_{0l}(x)}\,\frac{\sigma_{pl}}{k|\vec{r}-\vec{x}|}\exp[i(\omega_{0l}t - k\vec{s}_l\cdot\vec{x} - k|\vec{r}-\vec{x}|)] \tag{4}$$

where σ_{pl} is a scattering coefficient for that particle that specifies the intensity, phase shift and polarization of the scattered wave relative to the illuminating wave $\mathbf{E}_{0l}$. With the assumption that $\mathbf{x}\ll\mathbf{r}$, the vectors **r-x** and **r** are nearly parallel and by simple geometry:

$$|\vec{r} - \vec{x}| = r - \vec{x}\cdot\vec{r} \tag{5}$$

in the far field. Then:

$$\vec{E}_{pl} = \sqrt{I_{0l}(x)}\,\frac{\sigma_{pl}}{kr}\exp[i(\omega_{0l}t - kr + k\vec{x}\cdot(\vec{r}-\vec{s}_l))] \tag{6}$$

This equation implies that the scattered wave is approximately a spherical wave diverging from the origin whose phase depends on the particle position by the term $\mathbf{kx}\cdot\mathbf{s}_l$. The instantaneous frequency of a nearly sinusoidal signal is defined as the time derivative of its phase. From equation (6) this frequency is:

$$\omega_{dl}=\omega_{0l} + k\vec{v}(t)\cdot(\vec{r}-\vec{s}_l) \tag{7}$$

where v(t) is the velocity of the particle:

$$\vec{x}(t)=\vec{x}_0 + \vec{v}(t)t \tag{8}$$

The electric field generated at the far field by the scattered light can now be written as:

$$E_{pl} = \sqrt{I_{0l}(x)}\,\frac{\sigma_{pl}}{kr}\exp[i(\omega_{dl}t + k\vec{x}_0\cdot(\vec{r}-\vec{s}_l))] \tag{9}$$

In case of the dual beam back scatter principle, two laser beams intersect to form a measuring volume, see figure 5, in which a particle with position x(t) and velocity v(t) will scatter the light of both laser beam 1 (frequency ω_0) and of laser beam 2 (frequency $\omega_0+\omega_s$).

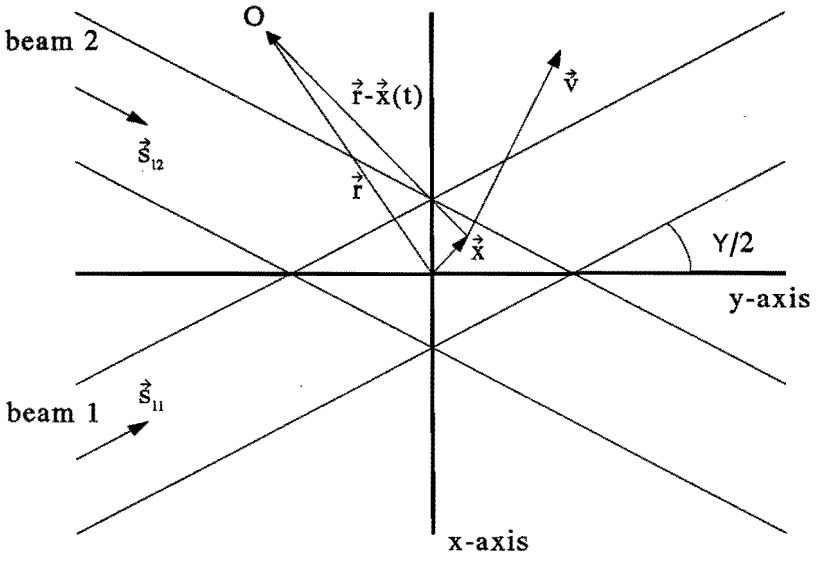

Figure 5. LDA dual beam back scatter principle.

Following the procedure described above the scattered light of the first laser beam at the photodiode generates an electric field:

$$\vec{E}_{pl1} = \sqrt{I_{0l1}(x)}\ \frac{\sigma_{pl1}}{kr}\exp[i(\omega_{d1}t + k\vec{x}_0\cdot(\vec{r}-\vec{s}_{l1}))] \tag{10}$$

where:

$$\omega_{d1}=\omega_0 + k\vec{v}(t)\cdot(\vec{r}-\vec{s}_{l1}) \tag{11}$$

For the second laser beam it follows that:

$$\vec{E}_{pl2} = \sqrt{I_{0l2}(x)}\ \frac{\sigma_{pl2}}{kr}\exp[i(\omega_{d2}t + k\vec{x}_0\cdot(\vec{r}-\vec{s}_{l2}))] \tag{12}$$

where:

$$\omega_{d2}=\omega_0+\omega_s + k\vec{v}(t)\cdot(\vec{r}-\vec{s}_{l2}) \tag{13}$$

The photodiode signal is now proportional to the intensity of the received light:

$$I = |\vec{E}_{pl1} + \vec{E}_{pl2}|^2 \tag{14}$$

Frequencies of the order of ω_0 can not be detected by the photodiode and result in a direct output V_0. The photodiode output signal has the form:

$$V = V_0 + \cos(\omega_d t + \phi) \tag{15}$$

Where ω_d is the Doppler frequency and can be written as:

$$\omega_d = \omega_{d1}-\omega_{d2} = \omega_s - \frac{2\sin(\frac{\gamma}{2})}{\lambda}v_x \tag{16}$$

where v_x is the component of v in the x direction. Equation (16) shows a linear dependence of the Doppler frequency on the velocity v_x of the particle and no dependence on the position of the photodiode. Therefore emitter and reciever can be united in one measuring probe and separate alignment is not necessary. A disadvantage of the back scatter method is that only a small part of the laser light is reflected in backward direction and a powerful laser and sensitive receivers are required.

For the LDA measurements an argon-ion laser 5500A of Ion Laser Technology is used. Emission takes place by electrical discharge. Three laser beams can be generated, a green (λ=488.0 nm), a blue (λ=514.5 nm) and a cyan one (λ=476.5 nm). The laser beams are linearly polarized. The power of the laser can be varied between 60 and 300 mW. Each laserbeam is splitted in a transmitter into two beams of the same intensity. One of these beams is shifted in frequency (40 MHz) in a Bragg cell, controlled by the flow velocity analyser (FVA). The laser beams are transmitted with the aid of glass fibers to a measuring probe. In this probe the laser beams are emitted and the reflected signal received. A front lens focusses the laser beams to form a measuring volume. In the two-dimensional case the green and blue laser beams are used. A photomultiplier transforms the optical signals into an electrical signal. This electrical signal is processed in the FVA and with the help of a personal computer and the software program FLOware a velocity signal is obtained (Kleuskens, 1992).

The dimensions of the measuring volume determine the spatial resolution of the Laser Doppler Anemometry setup. The focal length of the lens in the probe is 159.8 mm, the separation of the beams at the end of the probe is 38 mm and the diameter of the beam is 1.35 mm. The dimensions of the measuring volume in the experimental setup used are (figure 6):

$$dx = dy = 74\ \mu m, \qquad dz = 623\ \mu m \tag{17}$$

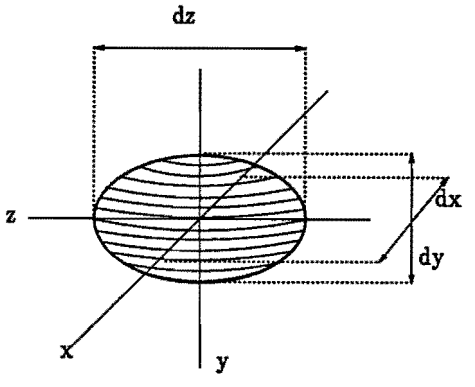

Figure 6. Dimensions of the measuring volume.

The resolution of the velocity is dependent on the frequency bandwidth, here 0.12 MHz. The resulting velocity range than extends from at least -0.1 m/s to 0.2 m/s. The velocity range is represented by 256 discrete points. Therefore the velocity resolution is equal to 0.002 m/s.

The Laser Doppler Anemometry in combination with the Flow Velocity Analyser (FVA) requires special data processing as the detection of a particle passing through the measuring volume is not uniform in time. The arrival times of the velocity measurements are therefore non-equidistant. As most literature and standard computer routines assume time series with equidistantial sample records a conversion has been made with the aid of an averaging method to an equidistant sample record (Gijsen, 1993).

APPENDIX C NUMERICAL METHOD

In this project the two dimensional unsteady free shear layer has been computed numerically using a finite element method. The finite element method used is described in this appendix. For the time dependent inflow the LDA measurements at station Y00 have been used.

C1. Governing equations

The two-dimensional Navier-Stokes equations for incompressible Newtonian fluids are given by the momentum equations together with the continuity equation:

$$\rho \frac{\partial \vec{u}}{\partial t} + \rho(\vec{u}\cdot\nabla)\vec{u} = \rho \vec{f} + \nabla\cdot\underline{\sigma} \tag{1}$$

$$\nabla\cdot\vec{u} = 0 \tag{2}$$

where ρ is the density and $\underline{\sigma}$ the Cauchy stress tensor:

$$\sigma_{ij} = -p\delta_{ij} + \eta\left(\frac{\partial u_i}{\partial x_j} + \frac{\partial u_j}{\partial x_i}\right), \qquad (i,j=1,2) \tag{3}$$

with p the pressure, δ_{ij} the Kronecker delta, u_i the i-th component of the velocity and η the dynamic viscosity.

C2. Spatial discretization

In order to discretize the governing Navier-Stokes equations the standard Galerkin method has been used. The velocity and pressure are at each time approximated by a linear combination of time-independent basis functions ϕ_{in} and ψ_m:

$$\tilde{u}_i = \sum_{n=1}^{N} u_{in}\phi_{in} \qquad (i,j=1,2) \tag{4}$$

$$\tilde{p} = \sum_{m=1}^{M} p_m \psi_m \tag{5}$$

The two-dimensional computational domain is subdivided into elements. The element used here is the modified Crouzeix-Raviart element, which consists of 7 nodes of which only the central node holds pressure unknowns, the pressure and its derivatives. By eliminating the velocity and pressure derivatives in the central node there are only 13 unknowns per element left (Cuvelier et al.,1986).

The following set of nonlinear ordinary differential equations is obtained (Cuvelier et al., 1986):

$$M\dot{\underline{u}} + [S + N(\underline{u})]\underline{u} + L^T\underline{p} = \underline{f} + \underline{b} \tag{6}$$

$$L\underline{u} = \underline{0} \tag{7}$$

where $\underline{u}$ is a vector of length 2N containing the velocity parameters u_{in} and $\underline{p}$ a vector of length M containing the pressure parameters p_m.
M is the mass matrix defined as (k=1,...,N and l=1,...,N):

$$M = \begin{bmatrix} M^{11} & M^{12} \\ M^{21} & M^{22} \end{bmatrix} \quad with\ M^{ij}(k,l) = \rho\delta_{ij}\int_{\Omega}\phi_{ik}\phi_{jl}d\Omega \tag{8}$$

S is the diffusion matrix (k=1,...,N and l=1,...,N):

$$S = \begin{bmatrix} S^{11} & S^{12} \\ S^{21} & S^{22} \end{bmatrix} \quad with\ S^{ij}(k,l) = \int_{\Omega}\eta[\sum_{\alpha=1}^{2}\left(\frac{\partial\phi_{ik}}{\partial x_\alpha}\frac{\partial\phi_{jl}}{\partial x_\alpha}\right)\delta_{ij} + \frac{\partial\phi_{ik}}{\partial x_j}\frac{\partial\phi_{jl}}{\partial x_i}]d\Omega \tag{9}$$

$N(\underline{u})\underline{u}$ is the nonlinear convective term (k=1,...,N and i=1,2):

$$[N(\underline{u})\underline{u}]_{ik} = \sum_{j=1}^{2}\int_{\Omega}\rho[\sum_{n=1}^{N}u_{jn}\phi_{jn}\sum_{l=1}^{N}u_{il}\frac{\partial\phi_{il}}{\partial x_j}]\phi_{ik}d\Omega \tag{10}$$

L is the divergence matrix (m=1,....,M and l=1,...,N):

$$L = [L^1\ \ L^2] \quad with\ L^i(m,l) = -\int_{\Omega}\psi_m\frac{\partial\phi_{il}}{\partial x_i}d\Omega \tag{11}$$

$\underline{f}$ is the force vector (k=1,...,N);

$$\underline{f} = [\underline{f}^1 \quad \underline{f}^2]^T \quad with \quad \underline{f}^i(k) = \int_\Omega \rho f_i \phi_{ik} d\Omega \tag{12}$$

and finally $\underline{b}$ is the boundary stress vector (k=1,...N) with Γ the contour of region Ω:

$$\underline{b} = [\underline{b}^1 \quad \underline{b}^2]^T \quad with \quad \underline{b}^i(k) = \int_\Gamma \sum_{j=1}^{2} \sigma_{ij} n_j \phi_{ik} d\Omega \tag{13}$$

The Newton-Raphson iteration is used for the linearization of the convective terms leading to (Van de Vosse, 1986):

$$N(\underline{u}^{n+1})\underline{u}^{n+1} = N(\underline{u}^n)\underline{u}^{n+1} + N(\underline{u}^{n+1})\underline{u}^n - N(\underline{u}^n)\underline{u}^n = J(\underline{u}^n)\underline{u}^{n+1} - N(\underline{u}^n)\underline{u}^n \tag{14}$$

with:

$$J(\underline{u}^n)^{ij}(k,l) = \frac{\partial}{\partial u^n_{jl}} [N(\underline{u}^n)\underline{u}^n]_{ik} \tag{15}$$

C3. Penalty function method

There are several ways to solve the set of differential equations (6) and (7). Using the direct solution method where pressure and velocity are being solved together at the same time, is time and memory consuming due to the absence of the pressure in the continuity equation, leading to a block of zero's on the diagonal of the system. To overcome this problem the penalty function method can be applied. The velocity vector is now related to the pressure by:

$$\nabla \vec{u} = \varepsilon p \qquad with \qquad \varepsilon \ll 1 \tag{16}$$

where ε is called the penalty function parameter. The solution of the set of equations solved with the penalty function method converges to the solution of the direct method.

C4. Time integration

The time derivative in the discrete Navier-Sokes equations can be approximated by a finite difference θ-method. Considering a simple equation:

$$\dot{\underline{u}} = \underline{f} \tag{17}$$

The approximation is defined by:

$$\frac{\underline{u}^{n+1} - \underline{u}^{n}}{\Delta t} = \underline{f}^{n+\theta} \tag{18}$$

with:

$$\underline{f}^{n+\theta} = \theta\underline{f}^{n+1} + (1-\theta)\underline{f}^{n} \quad \textit{with } 0 \le \theta \le 1 \tag{19}$$

Two methods can be distinguished: the Euler implicit method (θ=1) and the Crank-Nicholson method (θ=0.5). The latter is the most accurate $O(\Delta t^2)$ but is also inclined to increase oscillatory behaviour (Van de Vosse, 1986). Therefore for all computations a two step solution method has been used. The first step from t to t+½Δt is Euler implicit and unconditionally stable. The second step is an extrapolation from t+½Δt to time level t+Δt which is only conditionally stable.

All together this leads to solving the following equations:
first step:

$$[\frac{1}{\theta\Delta t}M + S + J(\underline{u}^{n}) + \frac{1}{\varepsilon}L^{T}M_{p}^{-1}L]\underline{u}^{n+\theta} = \frac{1}{\theta\Delta t}M\underline{u}^{n} + \underline{f}^{n+\theta} + \underline{b}^{n+\theta} + N(\underline{u}^{n})\underline{u}^{n} \tag{20}$$

$$\underline{p}^{n+\theta} = \frac{1}{\varepsilon}M_{p}^{-1}L\underline{u}^{n+\theta} \tag{21}$$

second step:

$$\underline{u}^{n+1} = \frac{1}{\theta}[\underline{u}^{n+\theta} - (1-\theta)\underline{u}^{n}] \tag{22}$$

APPENDIX D EXPERIMENTAL RESULTS

D1. Visualization experiments

The visualization of the free shear layer has been realized by injecting fluorescent dye in the upper flow. Stationary free shear layers have been visualized for different Reynolds numbers varying from 200 to 1000. This Reynolds number is based on the height of the flow channel where the two streams merge. It was seen that only for Reynolds numbers of 600 and higher flow instabilities occur. Next, unsteady free shear layers have been visualized, using the flow pulse described in appendix B. The Reynolds number of the diastolic phase was kept about 270 and increased during the systolic phase up to 1000. Different flow ratios have been visualized. In this section only the flow ratio Q_2:Q_1=1:3 is discussed, where Q_2 represents the bottom flow and Q_1 the upper flow. Since not many differences of the flow phenomena have been seen for different flow ratios and as a similarity between the physiological and experimental situation is desired, this flow ratio has been chosen. Figure 1 is a representation of the total flow pulse used for the visualization. Figure 2 shows the visualization of the free shear layer for several time steps in one period.

As seen from these pictures instability first occurs in the decelerating part of the systolic phase. A small perturbation with wavelength 1.6H (0.8 cm) is observed (see figure 2c). This perturbation grows in part of the diastolic phase and pairing can be seen (see figure 2f), since the wavelength of the vortices has increased to 3.2H and 4H (1.6 cm and 2.0 cm). The wavelength can be determined with an accuracy of ± 0.5H. Finally the perturbations are damped (see figure 2k,l and m). This process seems to correspond with transient stability as described in appendix A. The propagation velocity of the perturbations is approximately 1.4 v(dias) (4.5 cm/s), where v(dias) is the velocity at the end of the diastole at site Y00 (see figure 5).

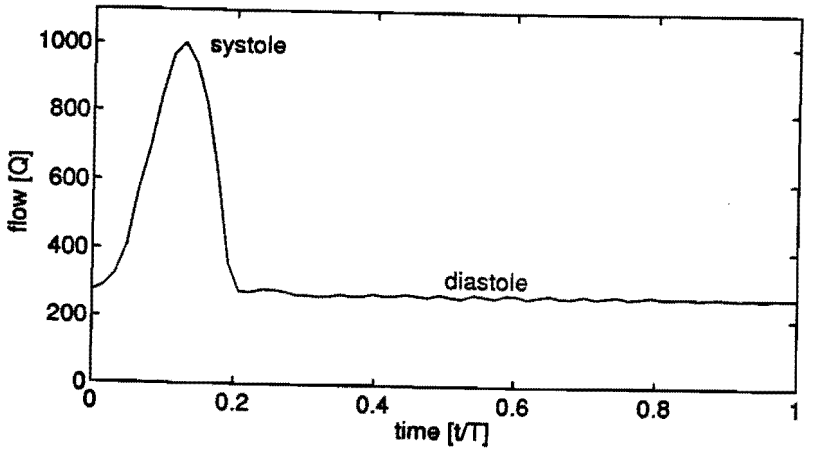

Figure 1. The experimental flow pulse.

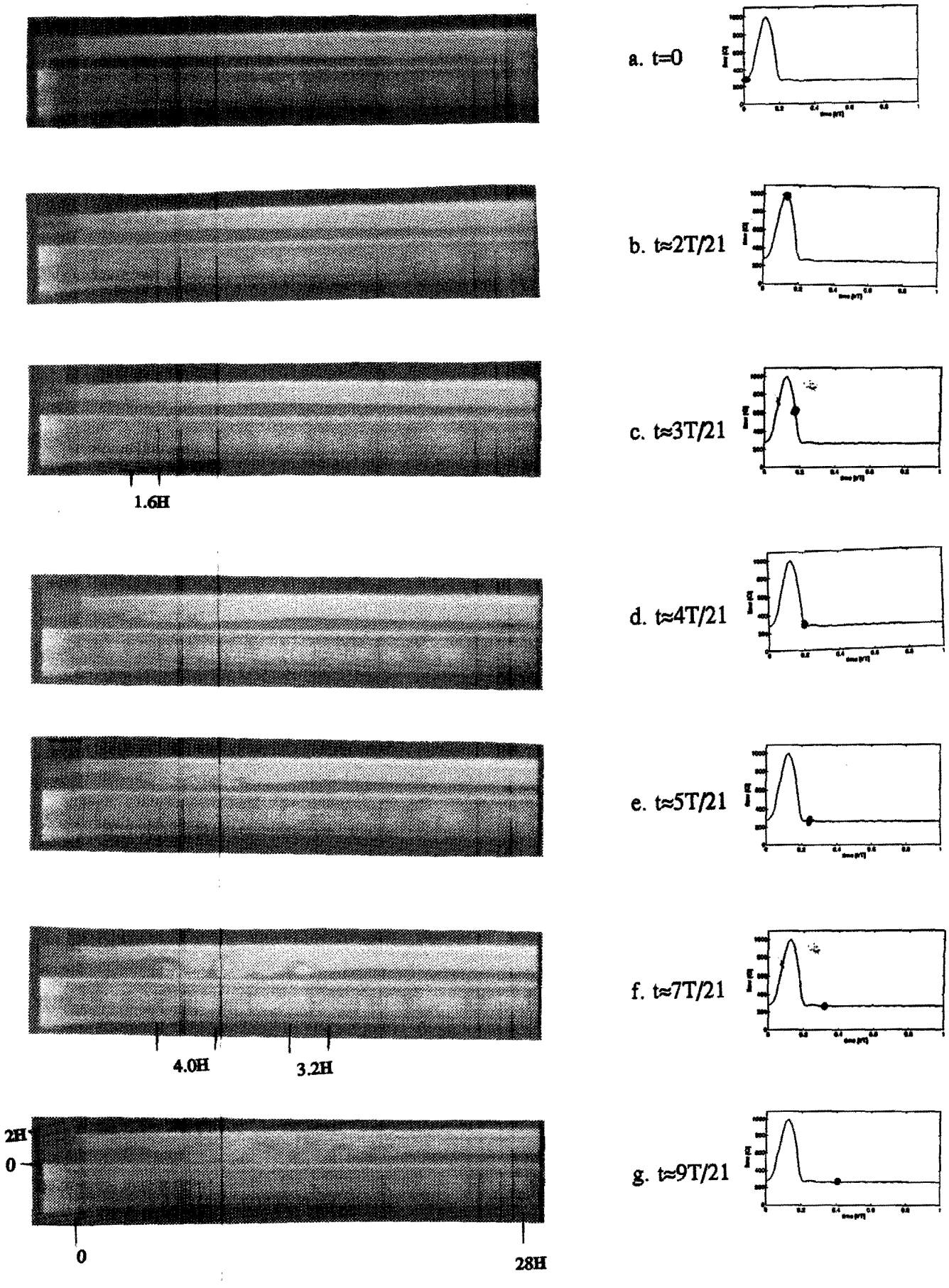
a. t=0
b. t≈2T/21
c. t≈3T/21
d. t≈4T/21
e. t≈5T/21
f. t≈7T/21
g. t≈9T/21
1.6H
4.0H
3.2H
2H
0
0
28H

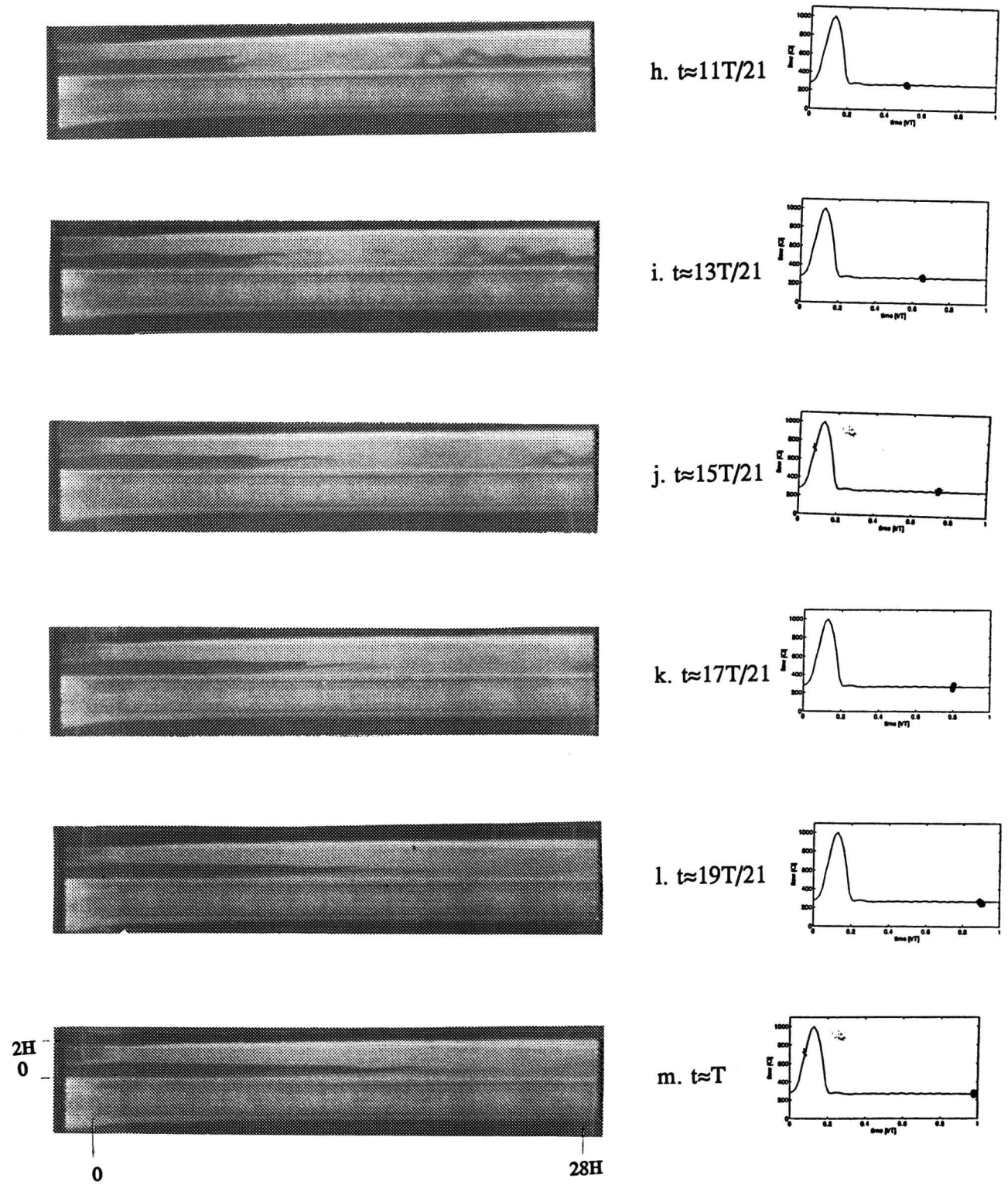

Figure 2. Results of the visualization experiments. Flow ratio 1:3.

D2. LDA experiments

D2.1. Experimental conditions

Laser Doppler Anemometry measurements have been made on the free shear layer for a flow ratio Q_2:Q_1 of approximately 1:3. The flow pulse is presented in figure 3 in which Q_1 and Q_2 represent respectively the upper flow and the bottom flow. The dimensionless parameters discussed in appendix B are: Re_{dias}=270, Re_{syst}=1000 and α=6. The systolic peak has the shape of a cosine occupying 20% of the period time and is superimposed on the steady flow as described in Appendix B.

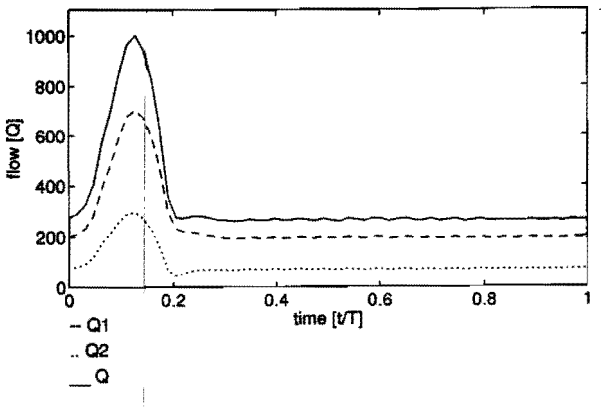

Figure 3. The flow pulse.

The flow ratio is not constant during a period as shown in figure 4. The approximate flow ratio of 1:3 is based on the ratio during the diastolic phase. During the systole the bottom flow Q_2 increases with respect to the upper flow Q_1. At the end of the systole the flow ratio is restored again after a dip in favour of the upper flow.

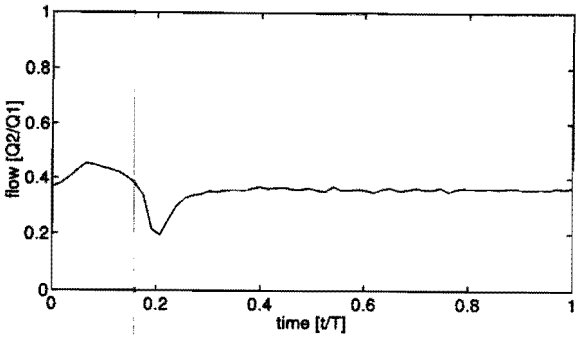

Figure 4. The flow ratio.

Figure 5 gives an overview of the measuring sites of the free shear layer. The measurements are taken along the y-axis or x-axis. The velocity has been measured in the x-direction, the axial velocity and in one case simultaneously in the y-direction, the secondary velocity. From the LDA velocity measurements equidistant time series are obtained following the procedure described in appendix B. The data are represented in a three-dimensional plot by normalized parameters. At the time-axis the actual time divided

by the period time is presented. The velocity parameter is normalized by dividing the actual velocity by the mean end diastolic velocity of the measuring site Y00. The position has been made dimensionless by dividing by half the height of the channel, therefore -1 defines the bottom wall and +1 the upper wall.

Also measurements have been made along the z-axis. From these measurements it was concluded that three-dimensional effects can be ignored when the measurements are taken near the center of the z-axis.

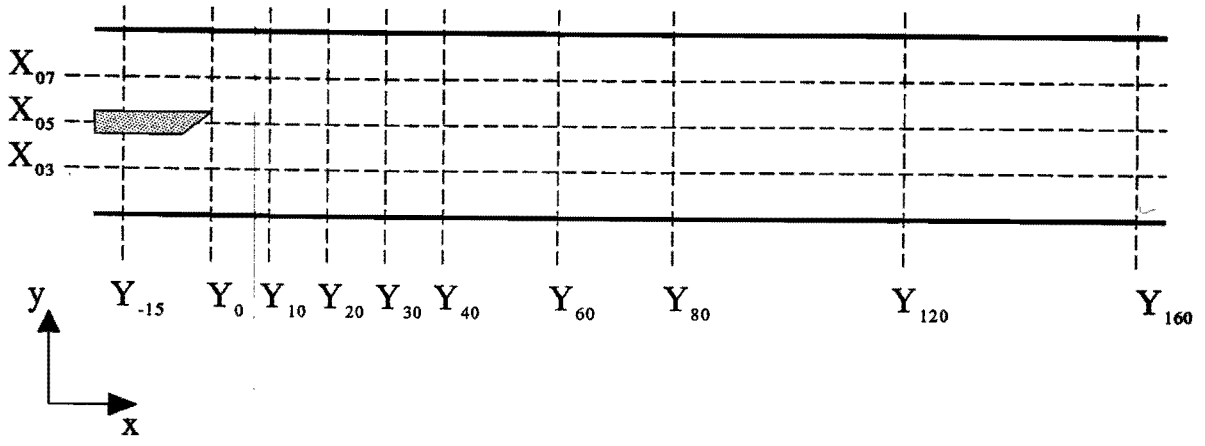

Figure 5. The measuring sites.

D2.2. Results

Y-15 The velocity profiles of the bottom and upper flow are nearly parabolic. The shape of the flow pulse can easily be recognized at this site. At the beginning of the diastolic phase a small oscillation can be seen.

Y00 The flow features are identical to those at Y-15, except for a small region of flow reversal at the bottom wall.

Y10 Near the bottom wall a rather steep velocity gradient during the decelerating phase of the flow pulse can be seen. This is followed by a region of flow reversal again followed by a much lower velocity peak at t/T= 0.3. At the high velocity region a gradually decreasing velocity during the decelerating phase of the systole towards the diastole is observed.

Y20 Still a region of flow reversal is seen near the bottom wall, followed by two oscillations. In the high velocity region after the systolic peak a second peak is being developed before the stationary conditions are reached during diastole. Two other small oscillations are seen in the diastolic phase.

Y30 At this site flow reversal is seen near both the bottom and upper wall. The region of flow reversal near the bottom wall is larger and growing. The small oscillation in the diastole now at t/T=0.4 has grown, especially in the upper half of the

channel. The second peak being developed in the high velocity region is moving towards the center of the channel. The flow is not parabolic any more but developed and more like the hyperbolic tangent velocity profile.

Y40 The region of flow reversal has become smaller near the bottom wall and has disappeared completely at the upper wall. Compared to site Y30 the second peak is larger in the center of the channel and the oscillation peak is higher at this site in the bottom half of the flow channel.

Y60 The systolic phase has been restored and is like the flow pulse again. The peaks of the oscillations are getting smaller and pass this measuring site at a later time. A velocity peak in the upper half of the flow channel appears together with a dip in velocity in the bottom half and reversed.

Y80 The oscillations have decreased. The total velocity profile has nearly developed to one parabolic velocity profile.

Y120 The oscillations have merely disappeared.

Y160 The oscillations have disappeared and the velocity signals are following the shape of the flow pulse even better than at site Y-15. A parabolic velocity profile has been developed.

In the following sites X03, X05 and X07 the velocity has been measured along the x-axis over 32H (16 cm). In figure 7 the axial velocities are given as a function of time. It is evidently seen that during the decelerating phase of the systole the first oscillations are being created within the first 10H (5 cm) downstream the separation plate. These oscillations travel forward with a propagation velocity of approximately 1.4H (4.5 cm/s) and are damped further downstream. At X05 the secondary velocity has also been measured. However these measurements have not given any additional information.

Apart from the accuracy of the LDA apparatus errors are introduced by several other aspects as random noise and the presence of a steep velocity gradient in intervals used for the averaging method to achieve an equidistant time series of data. Secondly an error is introduced by the interpolation whenever an interval contains no valid velocity measurements. Another source of errors is the fact that the traversing system of the measuring probe is not completely stable. The error made is maximally 8 %. Finally by computing the mean velocity over several periods the standard deviation has been calculated, see figure 8. It is seen that the highest inaccuracy, approximately 25 %, occurs there where the oscillations are. The standard deviation at other places, where no oscillations are observed varies between 1 % and 3 %. Figure 9 shows for several periods the axial velocity as a function of time at point (80,3). A phase difference between the oscillations is seen for different periods. By averaging over periods some information get lost. Near the separation plate the differences between several periods are a lot less.

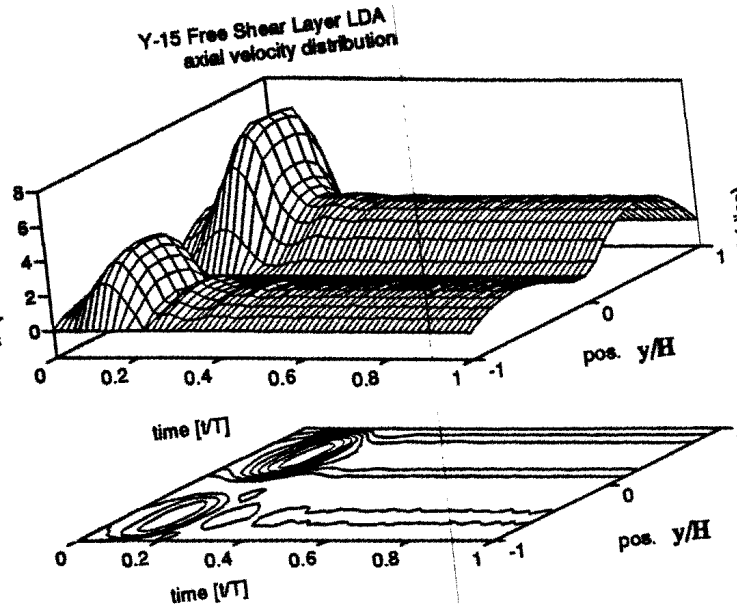
Y-15 Free Shear Layer LDA
axial velocity distribution
v/V(dias)
pos. y/H
time [t/T]

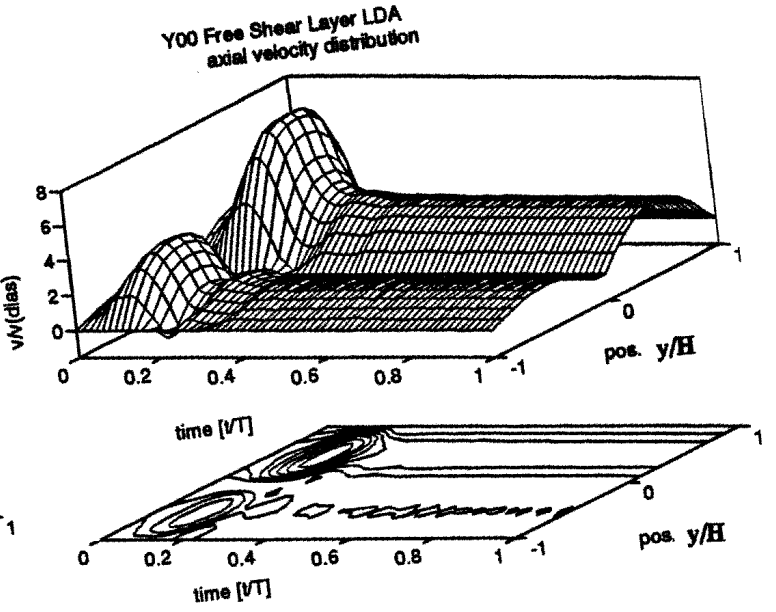
Y00 Free Shear Layer LDA
axial velocity distribution
v/V(dias)
pos. y/H
time [t/T]

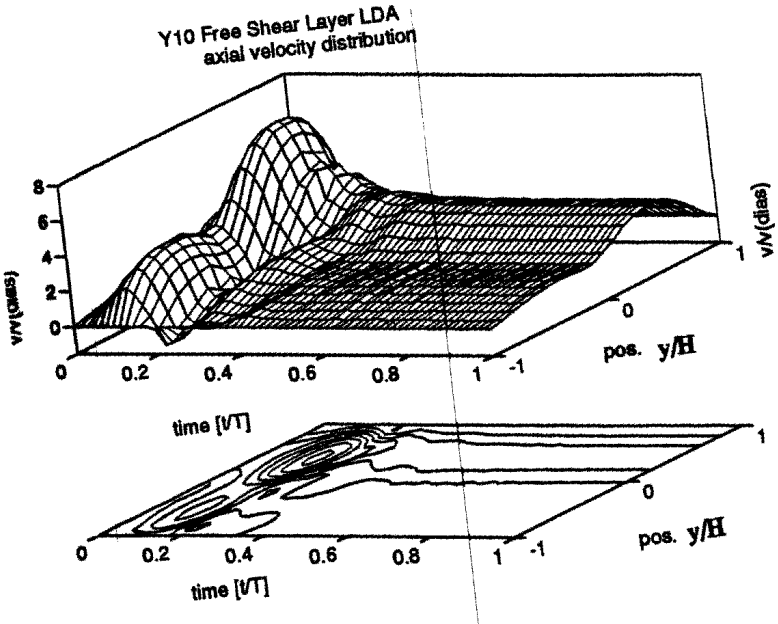
Y10 Free Shear Layer LDA
axial velocity distribution
v/V(dias)
pos. y/H
time [t/T]

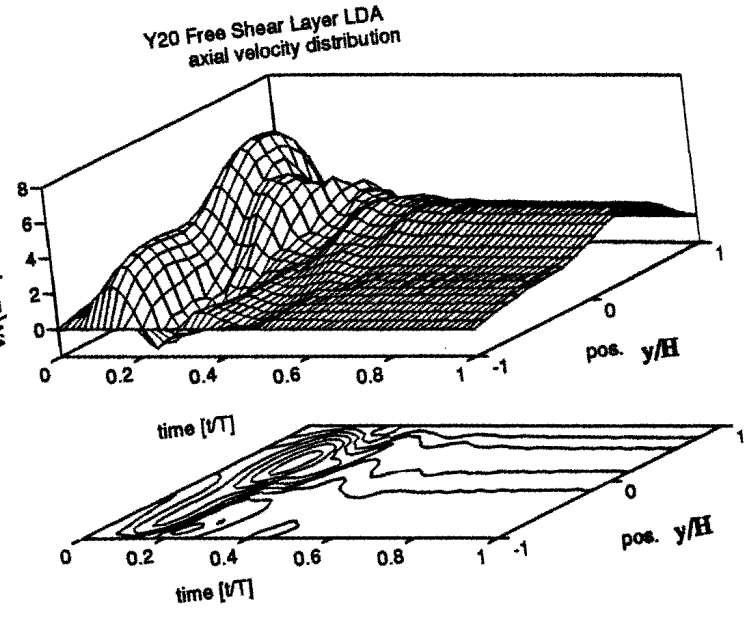
Y20 Free Shear Layer LDA
axial velocity distribution
v/V(dias)
pos. y/H
time [t/T]

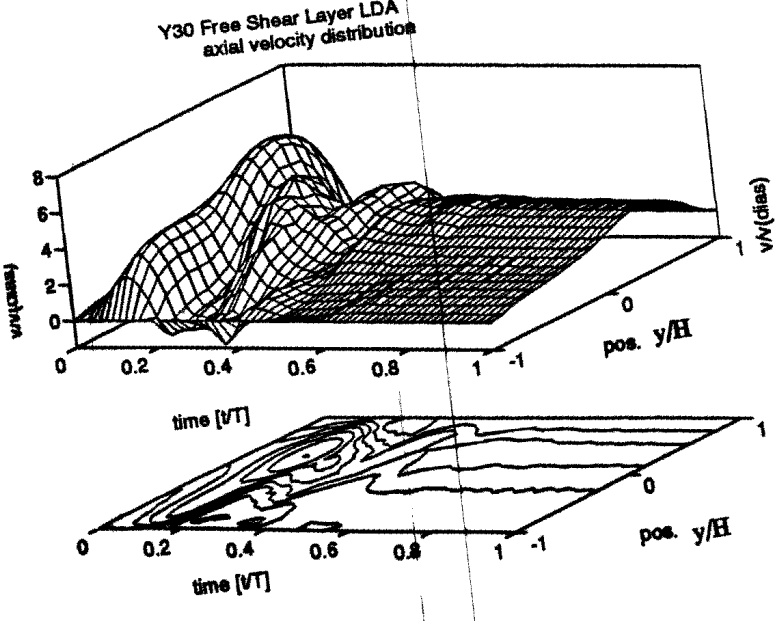
Y30 Free Shear Layer LDA
axial velocity distribution
v/V(dias)
pos. y/H
time [t/T]

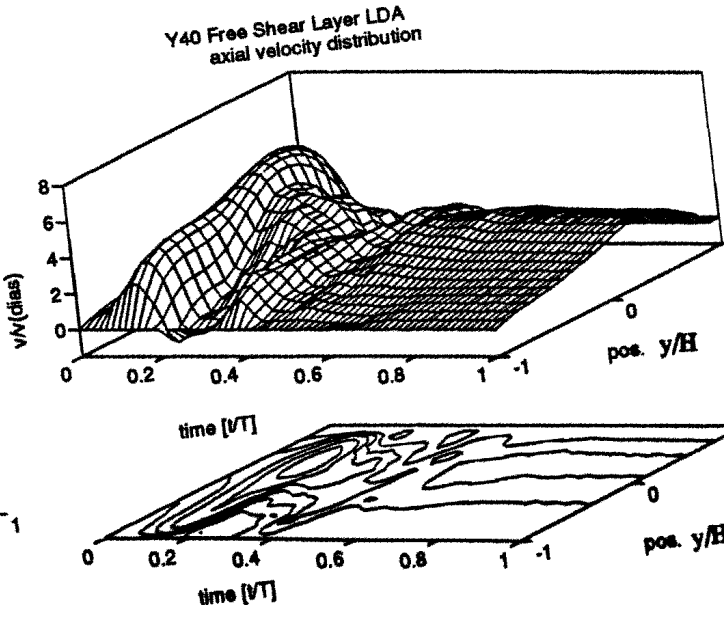
Y40 Free Shear Layer LDA
axial velocity distribution
v/V(dias)
pos. y/H
time [t/T]

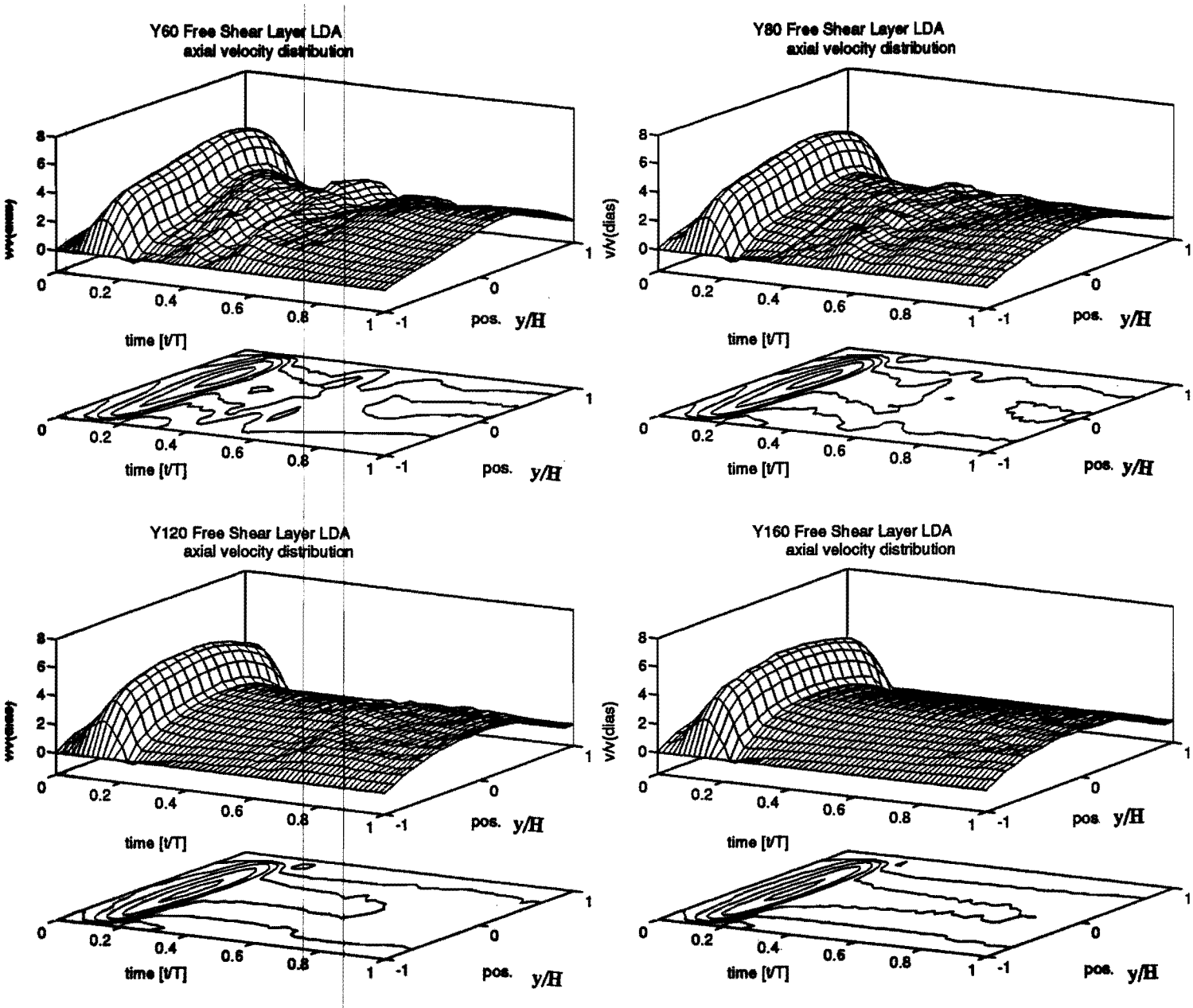

Figure 6. The axial velocities as a function of time measured along the y-axis for the LDA -measurements.

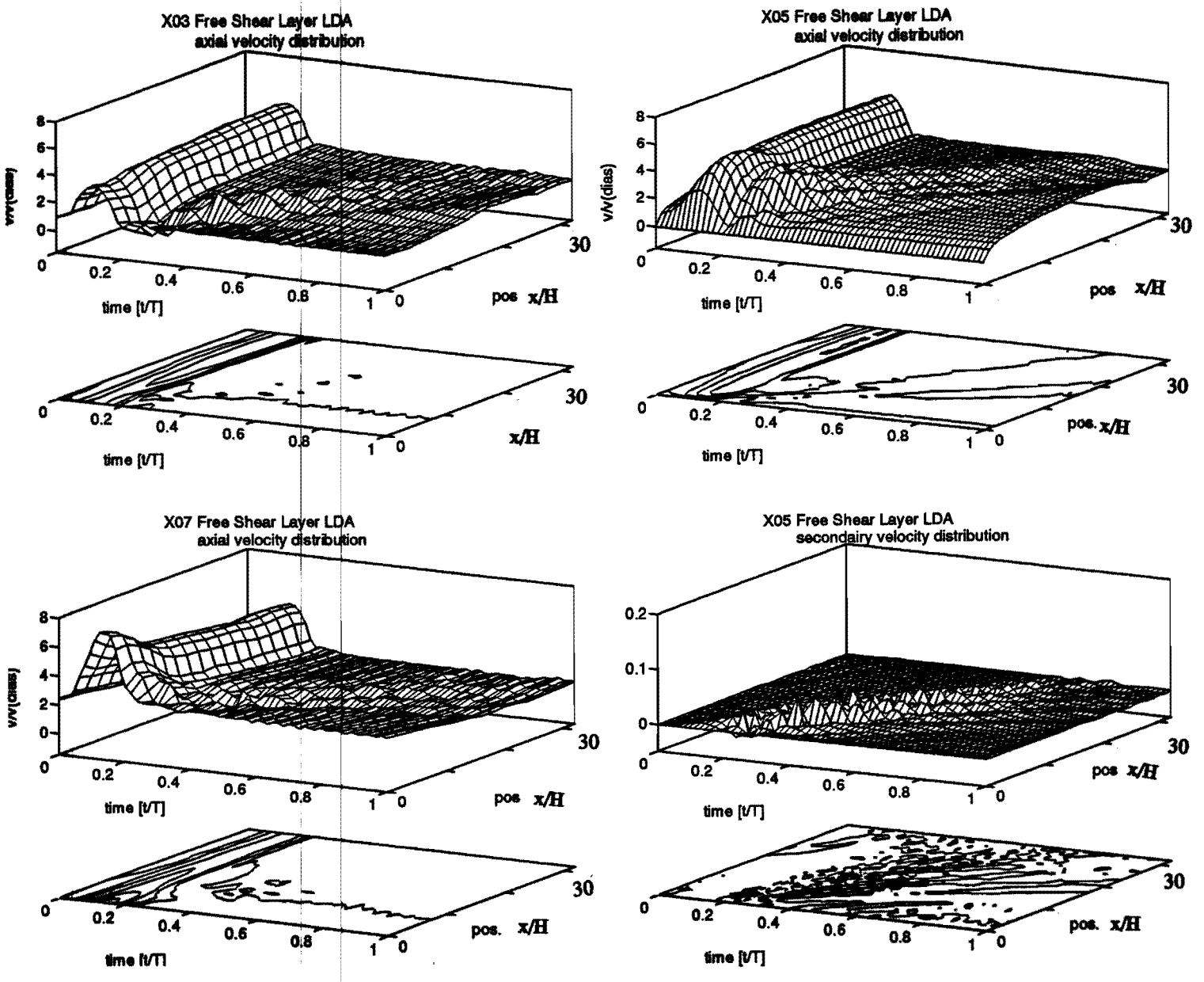

Figure 7. The axial velocities at X03, X05 and X07 and the secondary velocity at X05 as a function of time.

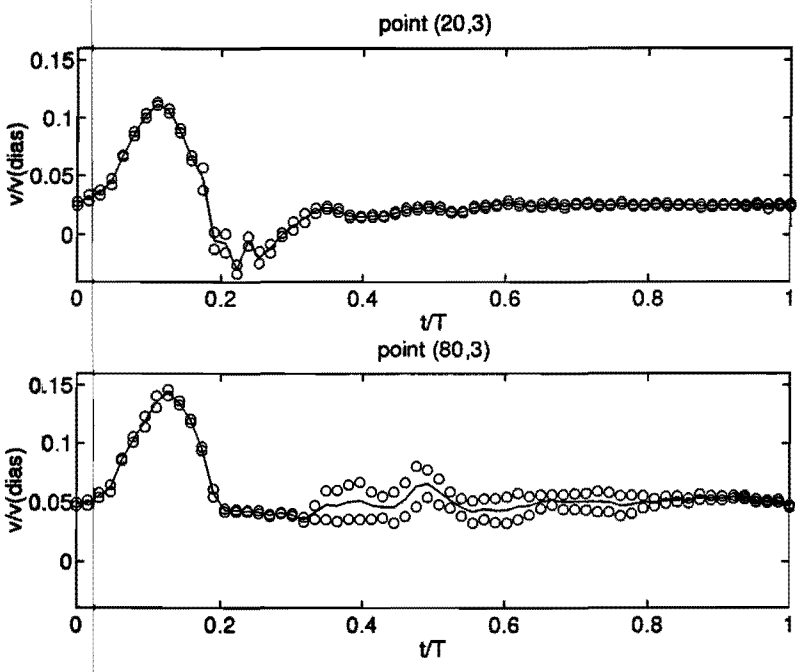

Figure 8. The mean velocity and its standard deviation at a certain point as a function of time.

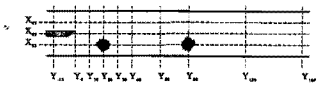

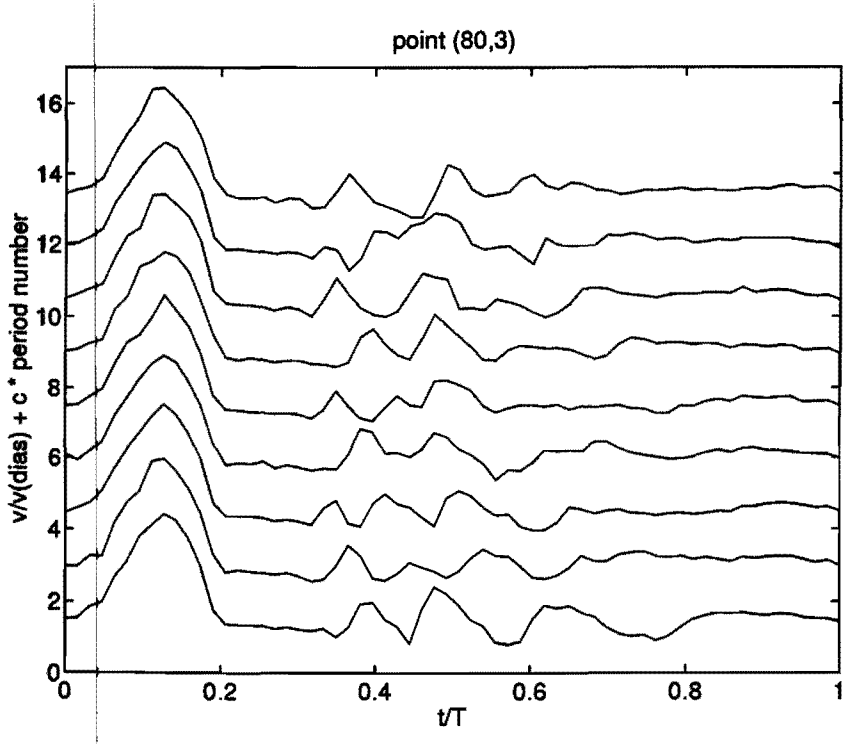

Figure 9. The axial velocity in point (80,3) as a function of time for several periods.

APPENDIX E NUMERICAL RESULTS

In this appendix the numerical results using the finite element method are given. As mentioned in appendix C the computational domain has been subdivided into elements. In this problem the modified Crouzeix-Raviart element has been used. The mesh is shown in figure 1.

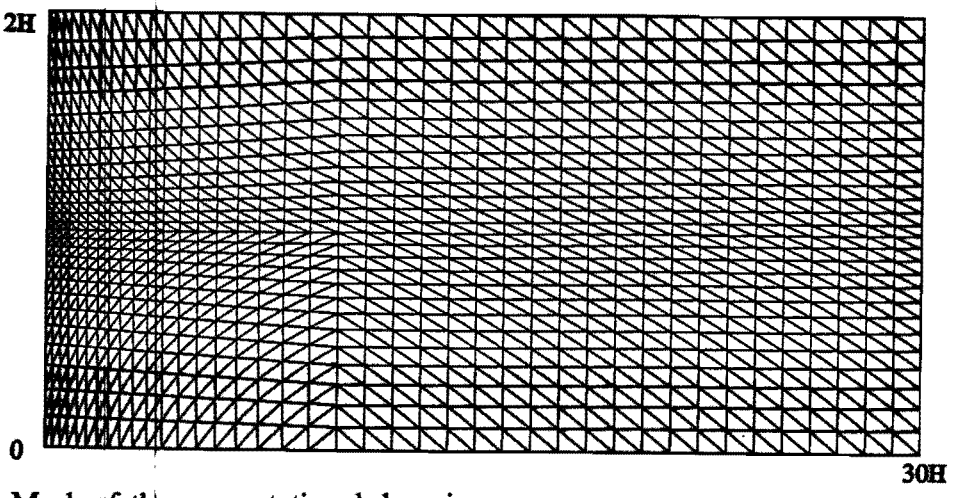

Figure 1. Mesh of the computational domain.

To provide an overall stable matrix in the computations the order of the velocity, density and the height of the channel is chosen of order O(1). Therefore these parameters have been scaled. A similar geometry as for the experiments has been used. The length of the channel is 30H, where 2H is the height of the flow channel. For the time-dependent inflow the LDA measurements at site Y00 have been used, see appendix D. At both walls the no-slip condition is valid and the outflow is determined by a zero stress-vector.

E1. Results

In order to compare both experimental and numerical results the numerical results have been represented the same way as the experimental LDA results, figure 2 and 3. These results are discussed below. The differences with the LDA measurements are stressed.

Y10 Near the bottom wall again a rather steep velocity gradient during the decelerating phase of the systole is seen, followed by a region of flow reversal. This is being followed by an oscillation at t/T=0.3. The high velocity region shows a gradually decreasing velocity during the decelerating phase of the systole. The phenomena are the same as for the LDA measurements but a little smoother.

Y20 At this site the same situation as at Y10 occurs except that in the high velocity region immediately after the systolic peak another peak is being developed. Oscillations are seen during the diastole. A velocity peak in the upper half of the flow channel occuring together with a dip in velocity in the lower half at the same time. Also at this site smoother profiles are obtained for the numerical computations as well as a smaller region of flow reversal near the bottom wall.

Y30 Flow reversal is also observed at the upper wall. The second peak in the high velocity region has grown, but has yet not moved towards the center of the channel as was seen for the LDA measurements. A much lower peak is observed in the bottom half of the flow channel in contradiction to the LDA measurements and again the regions of flow reversal are much smaller.

Y40 The regions of flow reversal have grown and it is as if the second peak has moved towards the center of the channel and other peaks also seem to have grown. In comparison with the LDA measurements a much higher peak is observed at the upper wall at $t/T \approx 0.35$. The perturbation near the bottom wall is less large at $t/T \approx 0.4$. The regions of flow reversal are much larger now. Two more oscillations are seen in the diastole.

Y60 The flow disturbances occur at this site at a later time in the period. The systolic phase has been restored. The peaks are higher than for the LDA measurements.

Y80 & Y120 The amplitude of the oscillations decreases. A nearly parabolic velocity profile has been developed. The peaks of the oscillations are higher compared to the LDA measurements and more regular.

At the sites X03, X05 and X07 it is clearly seen that during the decelerating phase of the systole several oscillations occur within the first 10H (5 cm). It can also be seen that further downstream the oscillations disappear again. The propagation velocity of the perturbations varies between 1.1 and 1.4 times v(dias) (3.6 and 4.5 cm/s).

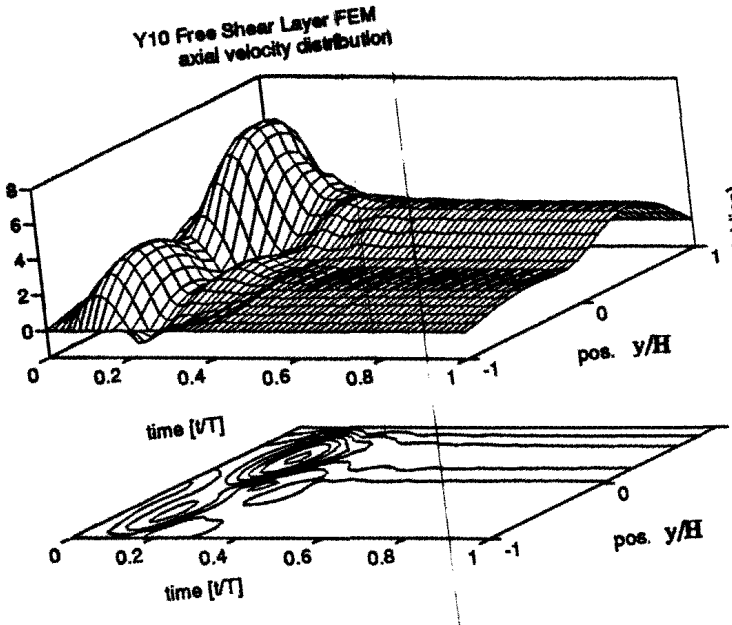
Y10 Free Shear Layer FEM
axial velocity distribution
v/V(dias)
pos. y/H
time [t/T]

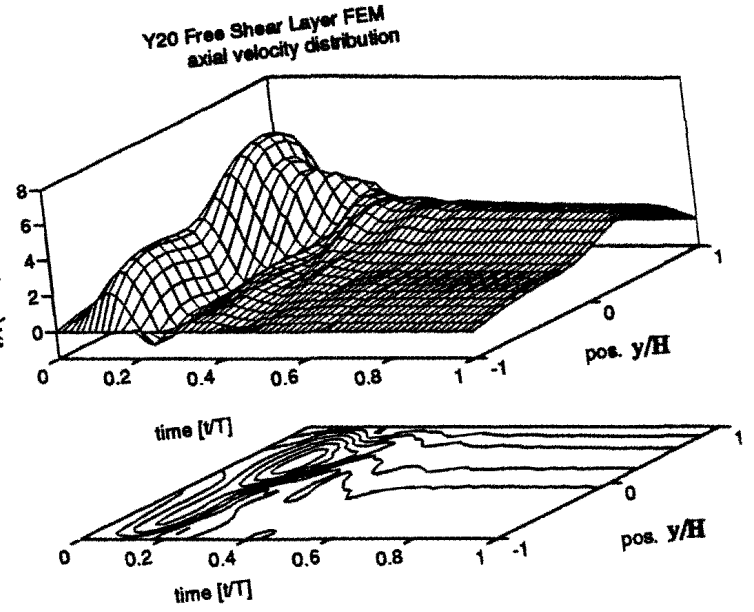
Y20 Free Shear Layer FEM
axial velocity distribution
v/V(dias)
pos. y/H
time [t/T]

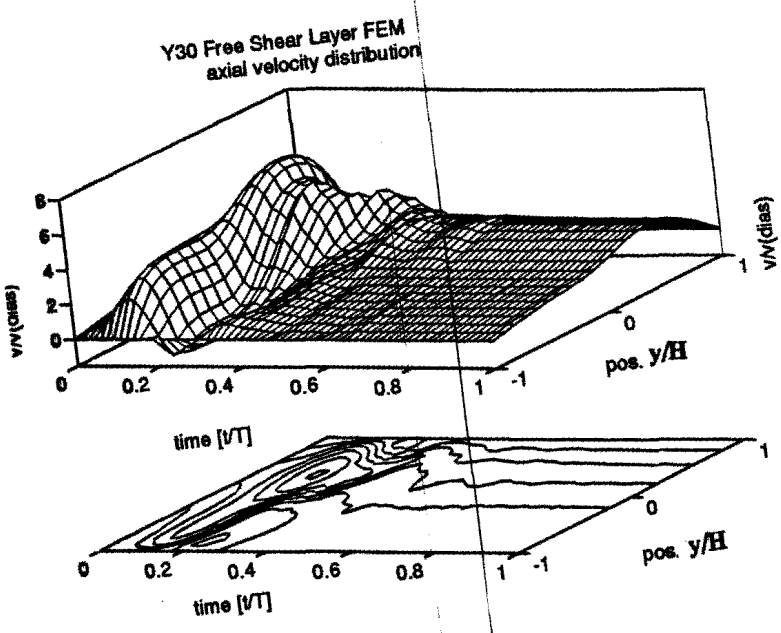
Y30 Free Shear Layer FEM
axial velocity distribution
v/V(dias)
pos. y/H
time [t/T]

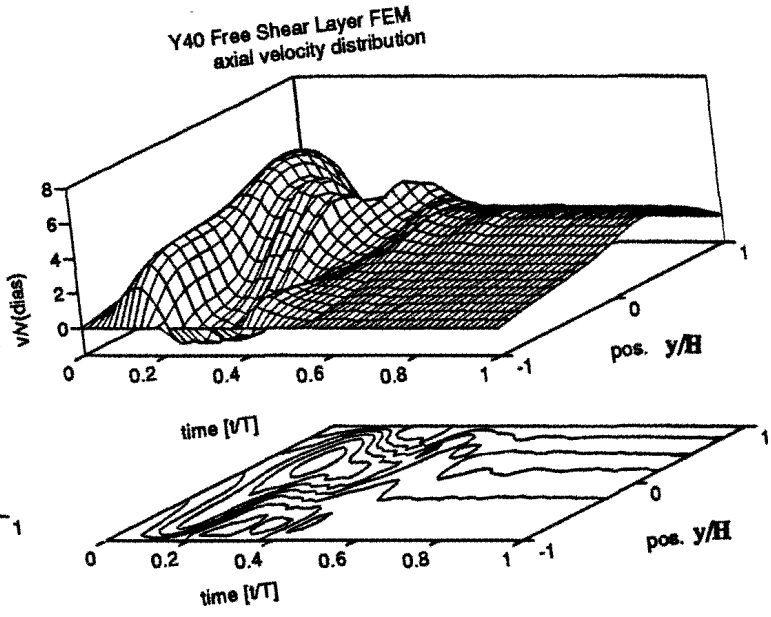
Y40 Free Shear Layer FEM
axial velocity distribution
v/V(dias)
pos. y/H
time [t/T]

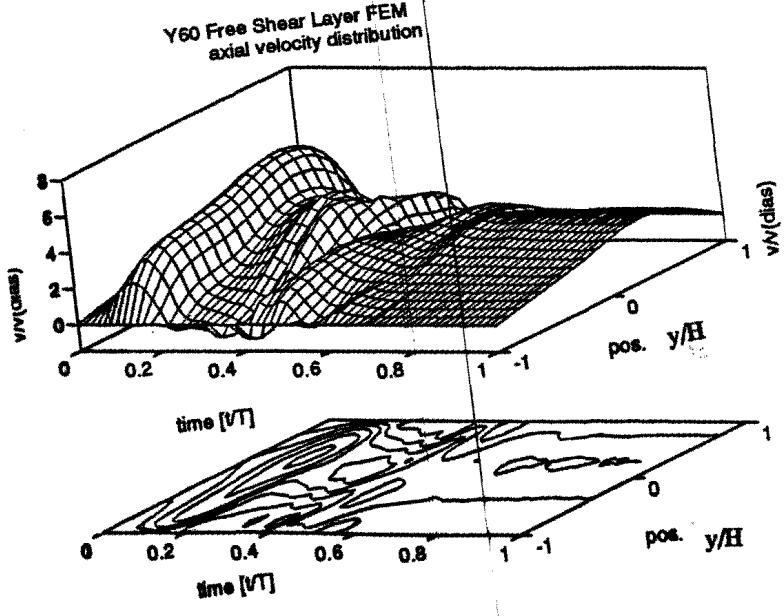
Y60 Free Shear Layer FEM
axial velocity distribution
v/V(dias)
pos. y/H
time [t/T]

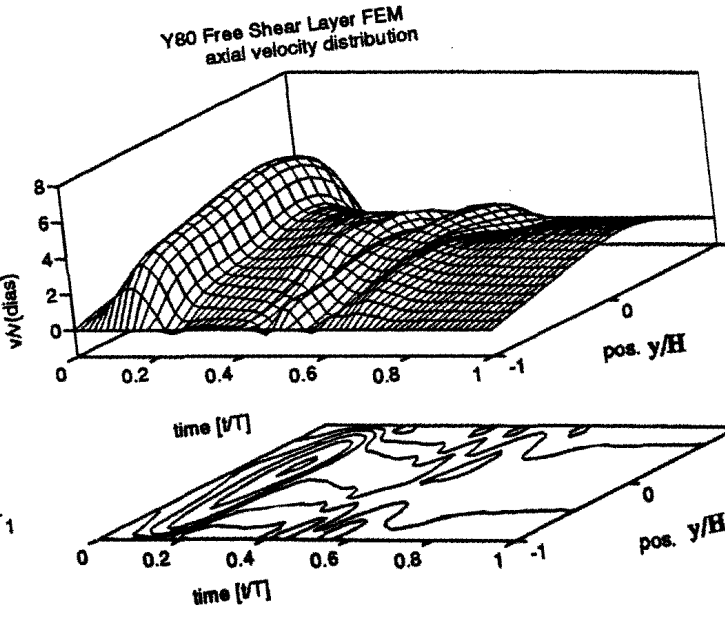
Y80 Free Shear Layer FEM
axial velocity distribution
v/V(dias)
pos. y/H
time [t/T]

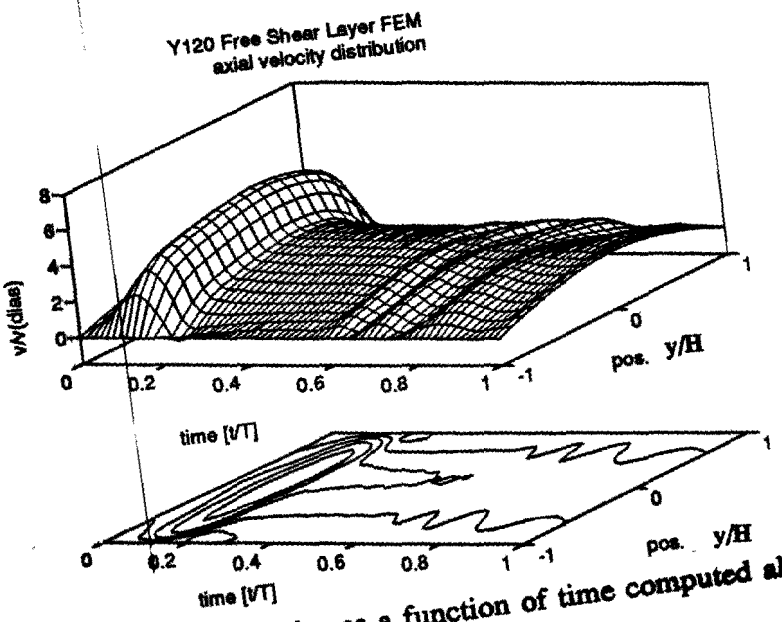

Figure 2. The axial velocities as a function of time computed along the y-axis.

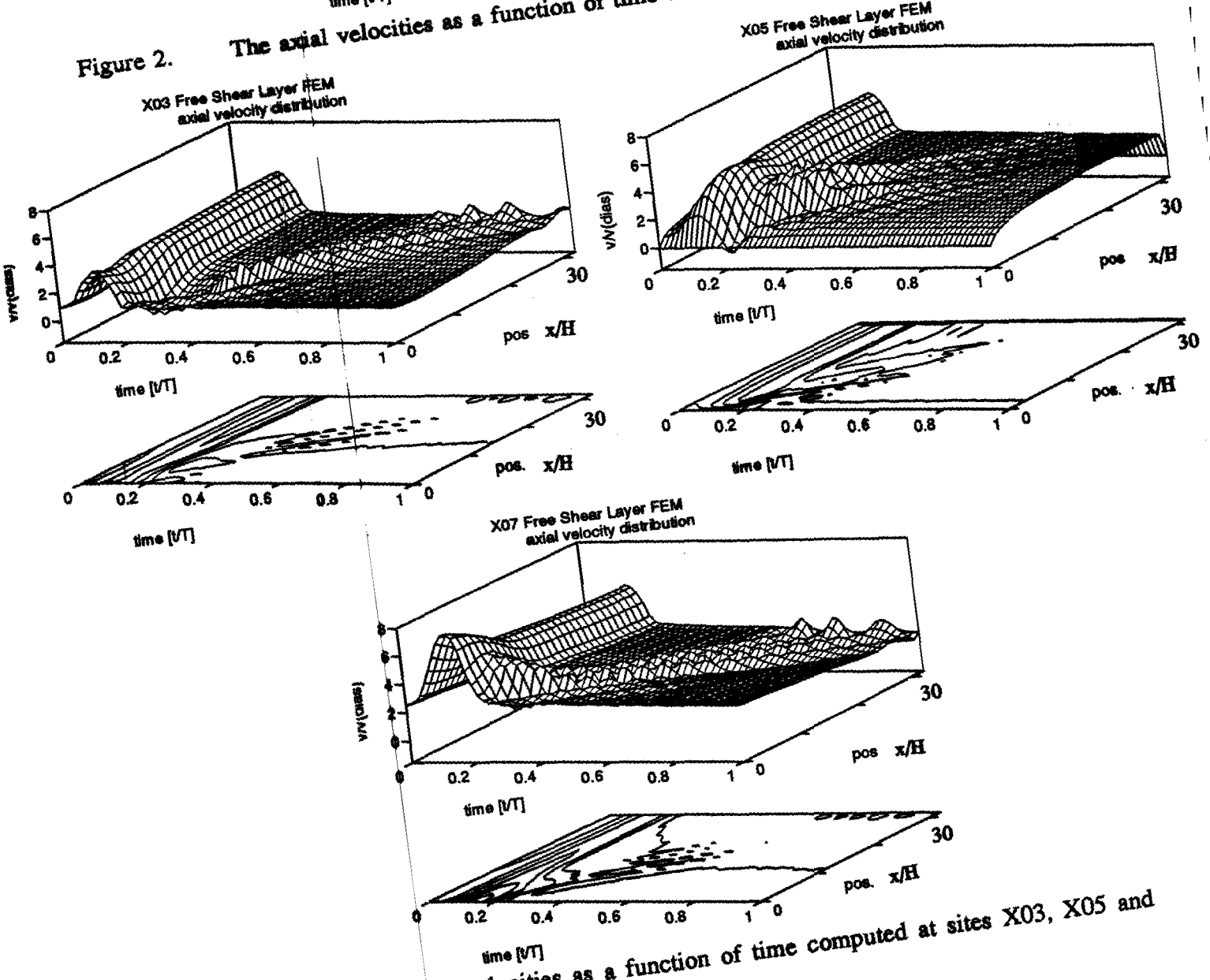

Figure 3. The axial velocities as a function of time computed at sites X03, X05 and X07.

E2. Instantaneous streamlines and the computed vorticity

In figure 4 the instantaneous streamlines of the numerical computations are given at the left-hand side of the figure. As here is dealt with unsteady flows the meaning of streamlines is not completely clear and the plots should be analysed carefully. Nevertheless it is believed that the contourlines of the streamfunction show where the velocity components are constant such that the occurrences of disturbances are visible in the instantaneous streamline plots. At the right-hand side the physically more meaningful quantity, the vorticity is plotted. In figure 4 the ratio of the height and length of the flow channel has been scaled with factor 5. From these plots it is seen that the first oscillations occur during the decelerating phase of the systole with perturbation wavelength of $\lambda = 1.6H$ (0.8 cm). The perturbations grow during part of the diastole and damp out again. Pairing of vortices occurs further downstream resulting in a wavelength of 3.2H (1.6 cm) and 4H (2.0 cm). The propagation velocity varies from 1.1 to 1.3 v(dias) (3.6 to 4.2 cm/s) during diastole and the propagation velocity is about 2.2 v(dias) (7.1 cm/s) at the systole. Thus approximately with the local velocity of the unperturbed flow.

It is seen that both the visualization and the computed instantaneous streamline plots provide the same information. Only in the streamline plots it was possible to obtain an approximation of the velocity of the perturbations during the systolic phase.

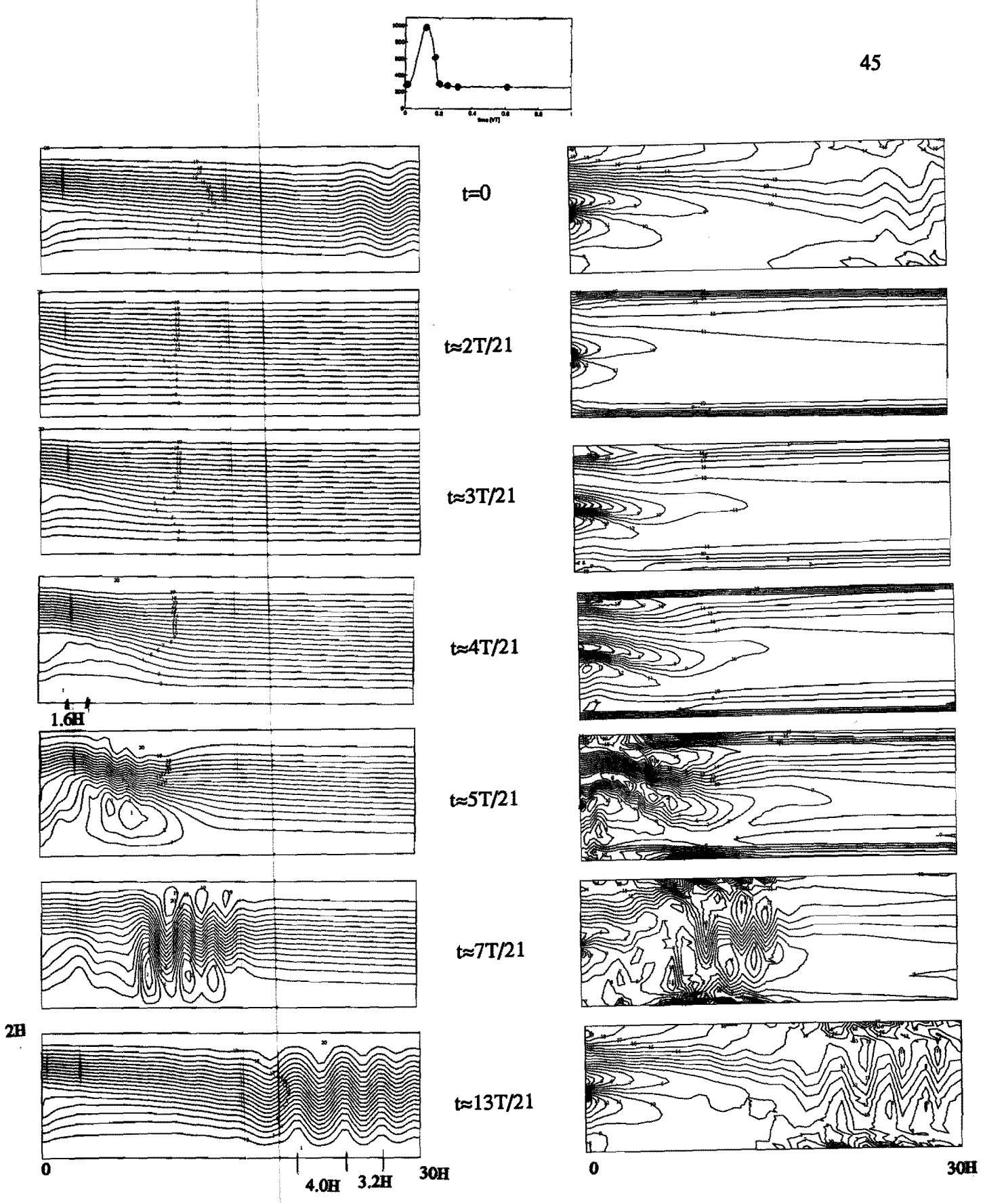

Figure 4. The instantaneous streamline plots for the numerical calculations (left) and the vorticity plots (right). The ratio of the height and length of the channel is scaled with factor 5. The flow ratio between the bottom and upper flow is 1:3.

APPENDIX F DISCUSSION AND CONCLUSIONS

Experimental techniques and finite element computations on a free shear layer flow have been compared in this paper. It is seen that the finite element method used provides good approximations of the shear layer as the experimental and numerical results agree rather well. A more quantitative comparison between the LDA experiments and the FEM computations is given in figure 1. Here the axial velocities in a few points are plotted as a function of time for both the LDA experiments as the FEM computations. It can be seen that the velocity at the diastolic phase of the flow pulse is a little higher for the LDA measurements probably due to the fact that the experiments are made in a three dimensional fluid circuit. The velocity profiles will also develop in the third dimension. The Reynolds number has been based on the total experimental three-dimensional flow. The largest differences are seen at the decelerating part of the systole with the highest velocity gradient and near the oscillations. This might be due to the fact that there is a large difference between periods where the oscillations are present in the flow pulse (see appendix D, figure 8 and 9). Here the mean velocity in a point is given as a function of time with its standard deviation for the LDA measurements. By the averaging over periods a loss in information of the oscillations occurs.

As is seen from the LDA measurements at site Y00 a small oscillation can already be seen before the two streams merge. It seems that there is a relation between this oscillation and the fact that the flow ratio is not constant over one period time of the flow pulse. It is assumed that a nonlinearity of the fluid circuit can be held responsible for the unsteadiness of the flow ratio and thus for the initial perturbation. If that is the case, the evolution of a forced perturbation has been studied. Finite element computations on the merging of two perfectly parallel pulsatile flows show that the phenomena that have been observed are very sensitive to the inflow conditions (see figure 2). Different wavelengths and less vortices can be observed. This might be a confirmation of the assumption mentioned above.

In the experimental geometry used here a separation plate is involved with a length of approximately 110H (55 cm) and boundary layers are developed at this plate. The effect of these boundary layers and thus the effect of the developed inflow velocity profiles is still unknown. As it is known that vorticity is usually generated in boundary layers their existence might be of great influence for the generation of the perturbations in a free shear layer and therefore should be studied carefully.

This discussion leads to the question what kind of instability is observed in the experiments and computations. Still the perturbations do not seem to be caused by vortex shedding at the tip of the separation plate. After all four vortices have been generated in the shear layer simultaneously within 10H downstream of the tip of the separation plate.

From the results presented in this paper it can be concluded that the transient stability of a shear layer with flow ratio 1:3 occurs, for a pulsatile unsteady flow. The first instabilities can be observed within 10H (5 cm) of the tip during the decelerating phase of the systole with perturbation wavelength 1.6H (0.8 cm) and seem to grow linearly. Further downstream nonlinear growth can be seen as pairing of vortices occurs. The wavelength grows to 3.2H (1.6 cm) and 4H (2.0 cm). The vortices are moving with approximately the

local velocity of the unperturbed flow. The presence of vortices with different wavelengths further downstream is assumed to be due to the fact that some vortices move with different velocity varying between 1.1 and 1.45 v(dias) (3.6 and 4.7 cm/sec). From this fact it can be concluded that spatial instability has been observed (Ho and Huerre, 1984).

The importance of this research is the relation with the flows through the carotid artery bifurcation, as there also occurs a free shear layer. Since perturbations observed here in the free shear layer are probably partly due to occurence of boundary layers at the separation plate the results can not directly be used for the shear layer in the carotid artery bifurcation. Besides, the flow in the carotid artery bifurcation is essentially three-dimensional. However further investigation on the influence of stenosis on the shear layer would possibly provide interesting information.

Finally it can be concluded that the FEM method is a rather good numerical method to simulate a free shear layer flow globally.

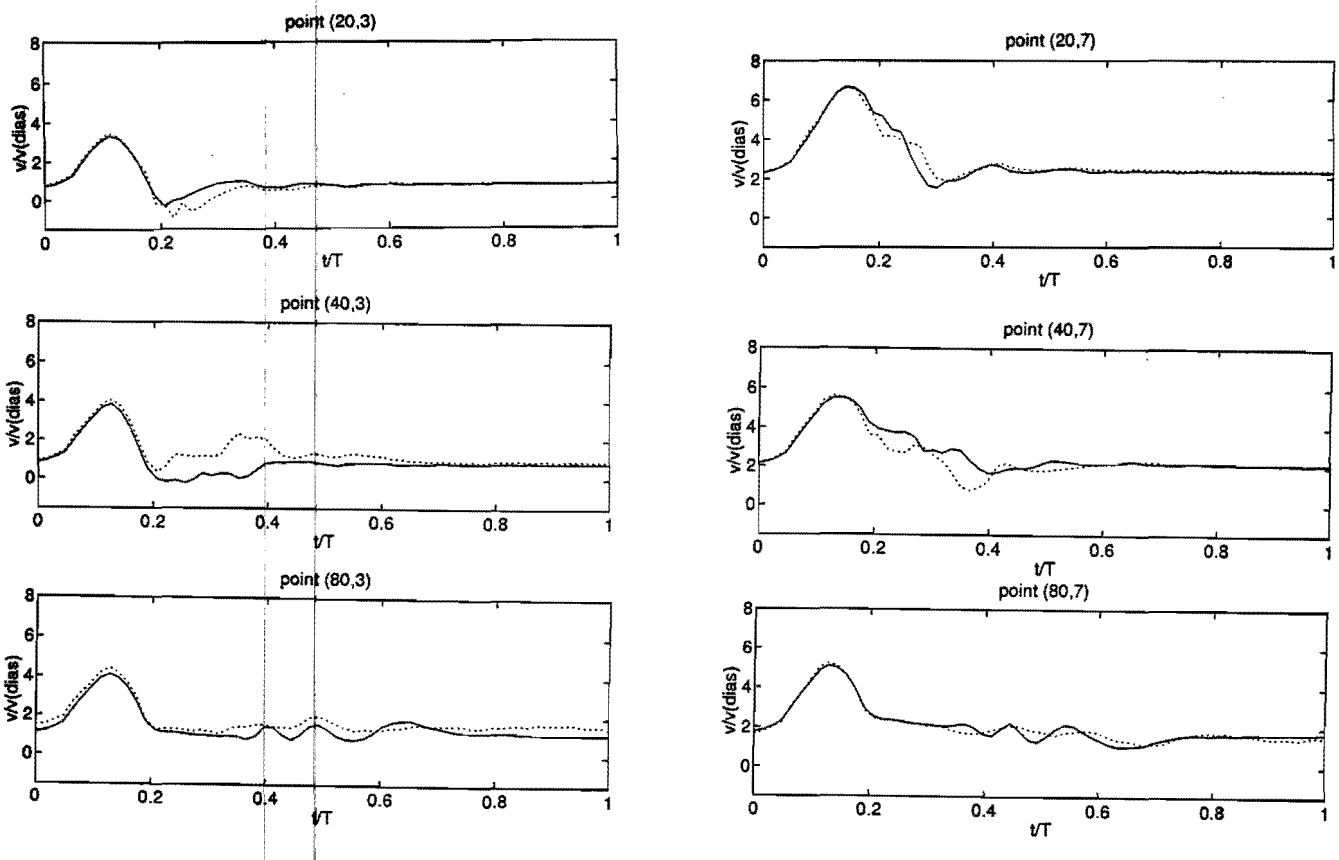

Figure 1. The axial velocities at a few points as a function of time for both LDA measurements (···) and FEM computations (___).

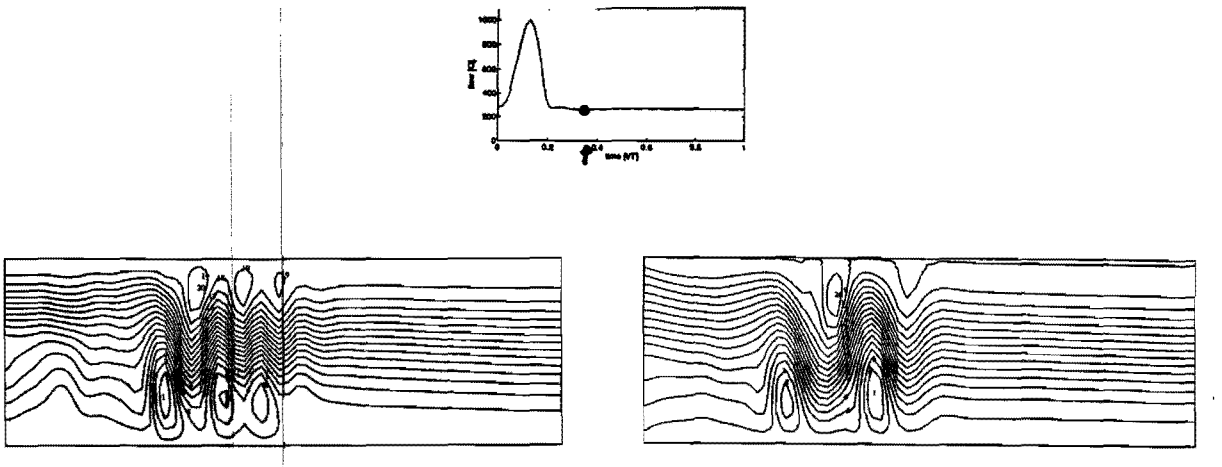

a. b.

Figure 2. Comparison between FEM computations with the measured velocity profile at Y00 as inflow condition (a) and for perfectly parallel flows (b)

References

[1] Betchov and Szewczyk (1963) Stability of parallel flows. New York: Academic Press.

[2] Cuvelier et al. (1986) Finite element methods and Navier-Stokes equations. D. Reidel Publishing Comp. Dordrecht/Boston/Lancaster/Tokyo.

[3] Davis (1976) The stability of time-periodic flows. Ann. Rev. Fluid Mech., volume 8, 57-74.

[4] Drazin and Reid (1981) Hydrodynamic stability. Cambridge University Press.

[5] Esch (1957) The instability of a shear layer between two parallel streams. J. Fluid Mech. 3, 289-303.

[6] Gijsen (1993) The influence of a mild stenosis on the flow field in the carotid artery bifurcation. LDA experiments. WFW report 93-043.

[7] Goldstein (1983) Fluid mechanics measurements. Hemisphere Publishing Corp.

[8] Ho and Huerre (1984) Perturbed Free Shear Layers. Ann. Rev. Fluid Mech. 16, 365-424.

[9] Kelly (1965) The stability of un unsteady Kelvin-Helmholtz flow. J. Fluid Mech. 22, 547-560.

[10] Kleuskens (1992) Laser Doppler Anemometry; The backscatter Fibre Optics Principle. internal report, WFW 92.071.

[11] Knio and Ghoniem (1990) Three-dimensional vortex simulation of roll-up and entrainment in a shear layer. J. Comp. Phys. 1990, 172-.

[12] Leonard (1980) Vortex methods for flow simulation. J. comp. Phys. 37, 289-335.

[13] Lie and Riahi (1988) Numerical solution of the Orr-Sommerfeld equation for mixing layers. Int. J. Engng Sci 26, 2, 163-174.

[14] Lin (1955) The theory of hydrodynamic stability. Cambridge University Press.

[15] Maslowe (1977) Weakly non-linear stability of a viscous free shear layer. J. Fluid Mech. 79, 689-702.

[16] Maslowe (1981) Shear flow instabilities and transition. Topics in applied physics 45, New York.

[17] Mehta et al. (1987) Comparison of experimenta and computational techniques for plane mixing layers. Phys. Fluids 30 (7), 2054-2062.

[18] Michalke (1964) On the inviscid instability of the hyperbolic-tangent velocity profile. J. Fluid Mech. 19, 543-556.

[19] Michalke (1965) On spatially growing disturbances in an inviscid shear layer. J. Fluid Mech. 23, 521-544.

[20] Miksad (1972) Experiments on the nonlinear stages of free-shear-layer transition. J. Fluid Mech. 56, 695-719.

[21] Palmen, v.d. Vosse, Janssen and v. Dongen (1992) The influence of minaor stenoses on the flow in the carotid artery bifurcation. Submitted to J. Biomechanics.

[22] Rindt, v. Steenhoven, Janssen, Reneman and Segal (1990) A numerical analysis of steady flow in a three dimensional model of the carotid artery bifurcation. J. Biomechanics 23, 461-473.

[23] Serrin (1959) On the stability of viscous fluid motions. Arch. Rat. Mech. Anal. 3, 1-13.

[24] Snijders (1993) Data processing of unsteady velocity measurements from the Dantec Flow Velocity Analyser, internal report WFW 93.016.

[25] Stuart (1960) Non-linear effects in hydrodynamic stability. Proc. 10th Intern. Congr.

Applied Mech., Stresa, Italy, 63-97.
[26] Vossers (1980) Stability, Lecture notes, Eindhoven University of Technology.
[27] V.d. Vosse (1986) Numerical analysis of carotid artery flow. Phd Thesis, Eindhoven University of Technology.